UNIVERSITY OF CALIFORNIA,
IRVINE

Graphene Based Transistors and Supported Lipid Bilayer

DISSERTATION

submitted in partial satisfaction of the requirements
for the degree of

DOCTOR OF PHILOSOPHY

in Chemical Engineering and Materials Science

by

Yung Yu Wang

Dissertation Committee:
Professor Peter John Burke, Chair
Professor H. Kumar Wickramasinghe
Professor Regina Ragan

2014

DEDICATION

To

my parents, brother and wife

Table of Contents

List of Figures

ACKNOWLEDGMENTS

I would like to thank my dissertation advisor, Professor Peter Burke, who provided me with his enthusiasm, inspiration, efforts and advices. This work would not have been finished without his help and guidance. It is my pleasure and honor to work with him.

I am also thankful to my dissertation committee members, Professor Kumar Wickramasinghe and Professor Regina Ragan for their valuable advices and discussions on my dissertation.

I thank all members of our group, Dheeraj Jain, Tae-Sun Lim, Nima Rouhi, Wei Wei Zhou, Katayoun Zand, Ted Pham, Phi Pham and Jinfeng Li for their supports, advices and help. They have been great co-workers, teachers, coworkers and friends offering me with passion, motivation and encouragement.

I also want to thank the team of INRF and Calit2 as well as the staff members at the Chemical Engineering and Materials Science at UC Irvine.

I am grateful to my friends at UC Irvine who have encouraged and supported me.

Most importantly, I would like to especially thank my family for their endless support, love and patience. I dedicate this thesis to them.

CURRICULUM VITAE

Yung Yu Wang

EDUCATION

UNIVERSITY OF CALIFORNIA, IRVINE Irvine, CA

Ph.D. Candidate in Chemical Engineering 2010 ~ 2014

UNIVERSITY OF SOUTHERN CALIFORNIA Los Angeles, CA

Master of Science in Chemical Engineering 2006 ~ 2007

- Relevant Course Work: Heat Transmission, Mass Transfer, Viscous Flow, Modeling and Analysis of Chemical Engineering System, Chemical Engineering Kinetics, and Thermodynamics

I-SHOU UNIVERSITY Kaohsiung, Taiwan

Bachelor of Science in Chemical Engineering 1999 ~ 2003

EXPERIENCE

Graphene and Carbon Nanotube – Peter J. Burke Research Group Irvine, CA

Research Assistant 2011 ~ 2014

- Fabricated CVD-grown graphene field-effect transistors by polydimethylsiloxane (PDMS) transfer process for biosensing applications
- Manufactured carbon nanotube field-effect transistors by standard photolithography process for biosensing applications
- Conducted silicon nano-wire field-effect transistors for ion channels sensing applications

The Laboratory for Electron and X-ray Instrumentation (LEXI) Irvine, CA

Laboratory Assistant 2011 ~ 2013

- Techniques support in materials characterization instruments such as AFM, XRD, SEM and TEM
- Trained users on sample preparation and instruments operation on AFM, XRD, SEM and TEM
- Conducted projects for companies on materials characterization in AFM, SEM and TEM

Nanomaterials and Solar Energy – Matt Law Research Group Irvine, CA

Research Assistant 2010 ~ 2011

- Synthesized nanocrystalline films for tandem dye-sensitized solar cell and water-splitting device

Kenmos Photovoltaic Co., Ltd. Tainan, Taiwan

Process Integration Engineer 2008 ~ 2010

- Estimated and built up manufacture processes of a-Si/a-Si tandem solar cell for a start-up company
- Optimized parameters of equipment to increase solar cell efficiency for PECVD, PVD and laminator
- Conducted research and development of new product for a-Si/a-SiGe tandem solar cell
- Implemented several projects for improving quality of products and reducing the cost of manufacture
- Evaluated and analyzed new materials for manufacture like ethylene vinyl acetate (EVA)
- Oversaw and solved whole processes' problems during manufacturing process

Biosynthetic Medicine – Jer-Yiing Houng Research Group Kaohsiung, Taiwan

Research Assistant 2001 ~ 2003

- Applied enzyme of yeast and E. coli to synthesize medicine and optimize reaction yield
- Conducted bench scale and scale-up fermentation, optimization and purification bioreaction process
- Participated in experimental design, evaluated new analytical methods and summarize results
- Utilized ultraviolet-visible spectrophotometer (UV/VIS) to examine the yield of bacteria
- Employed and operated high performance liquid chromatography (HPLC), gas chromatography (GC) to analyze the reaction product

- Led team in implementing research plan, duties included but are not limited to scheduling, structuring and conducting experimental plans and processes, reporting results, and providing potential solutions

Publications

- Yung Yu Wang and Peter J. Burke. "Polyelectrolyte multilayer electrostatic gating of graphene field-effect transistors." (Accepted in Nano Research).
- Yung Yu Wang, Ted D. Pham, Katayoun Zand , Jinfeng Li and Peter J. Burke. "Charging the quantum capacitance of graphene with single biological ion channel." *ACS Nano*, **2014**, 8 (5), 4228–4238.
- Yung Yu Wang and Peter J. Burke. "A large-area and contamination-free graphene transistor for liquid-gated sensing applications" *Applied Physics Letters*, **2013**, 103, 052103.
- Nima Rouhi, Yung Yu Wang and Peter J. Burke. "Ultrahigh conductivity of large area suspended few layer graphene films." *Applied Physics Letters*, **2012**, 101, 263101.
- Nima Rouhi, Santiago Capdevila, Dheeraj Jain, Katayoun Zand, Yung Yu Wang, Elliott Brown, Lluis Jofre and Peter J. Burke. "Terahertz graphene optics." *Nano Research*, **2012**,5, 667.

ABSTRACT OF THE DISSERTATION

Graphene Based Transistors and Supported Lipid Bilayer

By

Yung Yu Wang

Doctor of Philosophy in Chemical Engineering and Materials Science

University of California, Irvine, 2014

Professor Peter Burke, Chair

Graphene is an attractive material not only because of its electronic and optical properties, but also is considered for its potential applications in electronics and sensors. Owing to its unique structure and electrical property that are extremely sensitive to its surrounding environment, graphene-based field effect transistors (FETs) show significantly potential in various applications for chemicals and biomelocules sensors.

Here, we have demonstrated three different works. In the first project, we present a simple, low-cost, large area, and contamination-free monolayer graphene field-effect transistor for liquid-gated sensing applications. The graphene surface does not require any photoresist including the commonly used polymethylmethacrylate, thus avoiding possible contamination and mobility degradation. We also examine the effects of different etching solutions and concentrations on the Dirac point of graphene. With optimal device fabrication recipe, we demonstrate the device's capability to sense different KCl concentrations and pH values under liquid gating

configuration. Additionally, using polydimethylsiloxane as substrates holds an advantage of enabling simple integration between microfluidic systems and graphene for chemical and biological sensor applications.

In the second project, the interaction of cell and organelle membranes (lipid bilayers) with nanoelectronics can enable new technologies to sense and measure electrophysiology in qualitatively new ways. To date, a variety of sensing devices have been demonstrated to measure membrane currents through macroscopic numbers of ion channels. However, nanoelectronic based sensing of single ion channel currents has been a challenge. Here, we report graphene-based field-effect transistors combined with supported lipid bilayers as a platform for measuring, for the first time, individual ion channel activity. We show that the supported lipid bilayers uniformly coat the single layer graphene surface, acting as a biomimetic barrier that insulates (both electrically and chemically) the graphene from the electrolyte environment. Upon introduction of poreforming membrane proteins such as alamethicin and gramicidin A, current pulses are observed through the lipid bilayers from the graphene to the electrolyte, which charge the quantum capacitance of the graphene. This approach combines nanotechnology with electrophysiology to demonstrate qualitatively new ways of measuring ion channel currents.

In the third project, we apply polyelectrolyte multilayer films by consecutively alternative adsorption of positively charged polyallylamine hydrochloride and negatively charged sodium polystyrene sulfonate to the surface of graphene field effect transistors. Oscillations in the Dirac voltage shift with alternating positive and negative layers clearly demonstrate the electrostatic gating effect in this simple model system. A simple electrostatic model accounts well for the sign and magnitude of the

Dirac voltage shift. Using this system, we are able to create p-type or n-type graphene at will. This model serves as the basis for understanding the mechanism of charged polymer sensing using graphene devices, a potentially technologically important application of graphene in areas such as DNA sequencing, biomarker assays for cancer detection, and other protein sensing applications.

CHAPTER ONE

INTRODUCTION

1.1. BACKGROUND

1.1.1. PROPERTIES OF GRAPHENE

Graphene is a monolayer of carbon atoms structured as two-dimensional (2D) honeycomb lattice. The crystallite thickness is 0.34 nm for single layer of graphene. The carbon-carbon bond length is about 0.142 nm. Graphene is the basic structural element of some carbon allotropes including fullerenes, charcoal, carbon nanotubes and graphite. For electronic band structure graphene, it is a zero band gap semiconductor and the highest occupied molecular orbital (HOMO) overlaps the lowest unoccupied molecular orbital (LUMO) at a single point called Dirac point[1]. For electronic transport, the graphene has a remarkably high electron mobility (20,000 cm^2 V^{-1} S^{-1}) at room temperature. Additionally, the symmetry of the conductance indicates that the holes and electrons mobility is nearly the same. With a carrier density of 10^{12} cm^{-2} [2,3], the mobility of graphene is 200,000 $cm^2V^{-1}s^{-1}$ at the room temperature. The corresponding resistivity of the graphene sheet is 10^{-6} Ω cm which is the lowest resistivity known at room temperature.

1.2. PREPARATION METHODS OF GRAPHENE

1.2.1. MECHANICAL CLEAVAGE METHOD

First single layer of graphene was obtained by mechanical of graphite[4]. This method can obtain the highest quality of graphene sheet. The method of mechanical exfoliation is performed from highly oriented pyrolytic graphite (HOPG) which is composed of many stacked layers of

graphene. Because the carbon atoms of each graphene sheet are bonded by covalent bonds and the each graphene sheet of graphite is stacked by van der Waals (dipole-dipole) forces which are much weaker compared with covalent bonds, the layers of graphene can easily be removed from graphite bulk sample. The single layer of graphene can be obtained by using tape and pressing down to HOPG for few seconds. After the tape is peeled away, the thick layers of graphite stuck on it. Next, the clean adhesive section of the tape is used to press on graphite stuck for several seconds. After unfolding the tape, the two mirrored graphite are remained on the tape. This process is repeated until the color of graphite on the tape is changed from shiny to dark grey. This dark grey graphite on the tape is pressed firmly on the SiO_2 wafer substrate for several seconds. Then the tape is gently removed. Finally, the single layer or multilayer of graphene are formed on the SiO_2 wafer. However, the drawbacks of mechanical exfoliation method is not allowed to produce a large-sized graphene sheet which is limited to micrometer size.

1.2.2. EPITAXIAL GROWTH ON SILICON CARBIDE

Another method is epitaxial growth on SiC[5] substrate. This method can provide really high quality wafer scale graphene with 100GHz switching speeds. The graphene is grown on either high purity semi-insulating (HPSI) 4H(0001) 2" SiC wafers or semi-insulating (SI) 6H(0001) 2" SiC wafers in a UHV chamber (~$3x10^{-10}$ Torr). First, the SiC wafers is cleaned by annealing at 810℃ in Argon. After the cleaning step, the SiC wafer is annealed at 1450℃ for 2 min under Ar flow at a pressure of $3.5x10^{-4}$ Torr. But SiC substrate is annealed under high temperature (>1000 ℃) and ultra high vacuum. These will cause very high cost on materials and equipment.

1.2.3. CHEMICAL VAPOR DEPOSITION (CVD)-GROWN GRAPHENE ON NI METAL SUBSTRATES

Graphene film is formed by ambient pressure chemical vapor deposition (APCVD) on Ni coated Si substrates[6-8]. First, the Ni substrate is annealed at 900℃ under Ar and H_2 (600/400 sccm) for 20 min. The temperature is raised to 1000℃ with methane and hydrogen (3/1400 sccm) for 5 min. The as-grown graphene film is obtained on top of Ni substrates. In order to transfer graphene onto the target substrates, the as-grown graphene is spin-coated with a thin layer of poly(methylmethacrylate) (PMMA) which is about 200 nm thick. After PMMA coating, the sample is heated at 120℃. Then the Ni is etched away by Ni etchant for 4 h. The PMMA/Graphene film is transferred to DI water for cleaning etchant. After cleaning with DI water, the PMMA/Graphene film is transferred to the target substrates and dried at room temperature. Finally, the sample is annealed at 450℃ for 30 min in a Ar/H_2 atmosphere to remove the PMMA layer.

1.2.4. CHEMICAL VAPOR DEPOSITION (CVD)-GROWN GRAPHENE ON CU METAL SUBSTRATES

Chemical vapor deposition (CVD)-grown graphene on metal substrates such as Cu is the most reliable, inexpensive and efficient approach for transferring high-quality (such as mobility up to 7350 $cm^2 V^{-1} s^{-1}$), uniform and large-area (up to 30 inches) monolayer graphene which can

provide a good quality of graphene sheet for large sensing area and easy fabrication of sensor devices.

The methods of CVD growth and transfer of the graphene film were developed by Ruoff et al[9]. A single layer of graphene is grown on 25-μm thick Cu foils in quartz furnace. The Cu foil is heated to 1000℃ and maintain a H_2(g) pressure of 40 mTorr under 2 sccm flow. After the temperature is stable, 35 sccm of CH_4 is introduced for a desired period of time at a total pressure of 500 mTorr. Then the furnace is cooled to room temperature. After the growth process, poly-methyl methacrylate (PMMA) is spin-coated on the Cu foil. The Cu foil is etched by a 0.05 g/ml iron nitrate solution over night. After etching, the graphene film is transferred to DI water to remove the residual etchant. Then graphene film is transferred onto target substrate. Finally, the PMMA is dissolved by acetone.

1.3. CHARACTERIZATION OF GRAPHENE

There are a variety of techniques having been used in the characterization of graphene such as X-ray diffraction (XRD), X-ray photoelectron (XPS), atomic force microscopy (AFM), scanning electron microscopy (SEM), transmission electron microscopy (TEM), scanning tunneling microscopy (STM) and Raman spectroscopy. These techniques can be used to the characterization of structures, crystal structure, chemical compositions and morphology. However, in our research area, the Raman spectroscopy is the most useful technique to obtain the information about the quality graphene and the number of layers.

For graphene, the major features of the Raman spectra is the 2D band at ~2680 cm^{-1} and G band ~1580 cm^{-1}. The 2D band is due to second-order two-phonon mode and the G band is the E_{2g} vibrational mode. The D band at ~1350 cm^{-1}, is used to observe the defects of graphene. Higher intensity of D band means lower quality of graphene. Usually, the defects are cracks and tears which cause during CVD-grown and graphene transfer process. By using the ratio of 2D, G and D band intensity, the number layers of graphene can be determined. When the ratio of I(G)/I(2D) is ~0.3, ~0.5 and ~0.7, the number layers of graphene are 1, 2 and 3, respectively.

1.4. PROPERTIES OF LIPID BILAYER

The lipid bilayer is formed by two layers of lipid molecules which have a hydrophilic head and two hydrophobic tails. When lipid molecules are exposed to water, they will naturally form a two-layered sheet with all their hydrophobic tails forming toward inside of the two-layered sheet and all their hydrophilic head forming toward either side of two-layered sheet. This self-assemble to two-layered sheet is call hydrophobic effect. They held together by non-covalent forces. There are no chemical bonds forming between lipid molecules.

These two-layered sheet is a continuous about 5 nm thick barrier which can prevent ions, proteins and other molecules to pass through. However, by modifying lipid bilayer with protein pores, this can generate a channel or pathway for the flux ions or other molecules across lipid bilayer. Because lipid bilayer can easily combine with varieties of protein pores, this characteristic and function make lipid bilayer become very powerful and important tool for biosensor in application of sensing, signaling and communication.

1.5. OVERVIEW

For employing graphene sheet on chemical and biological sensing application, the clean graphene surface is very important. However, graphene surface is unavoidably contaminated by transfer and fabrication process. Therefore, we present a simple and low-cost fabrication of graphene field-effect transistor on PDMS which provides contamination-free and large area monolayer graphene film for liquid-gated sensing applications. Single layer graphene is transferred by PDMS; then the PDMS is directly used as substrate for device fabrication. The channel length of the transistors can be larger than 5 mm. This device avoids any chemical contamination during graphene transfer and fabrication. Therefore, a clean and high quality graphene surface is provided for investigation in variety of chemical and biological materials.

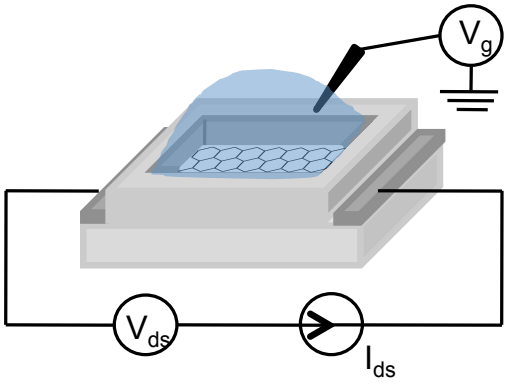

Figure 1.1. Schematic illustration of single layer graphene field-effect transistor on PDMS. substrate.

After first work is done, the graphene device is employed to combine supported lipid bilayers, with an aim to use the advantages of each technique to compensate for the shortcomings of the other and consequently present a novel approach to sensing single ion channel activity. In short, graphene will serve as the new sensing material while supported lipid bilayer will provide a medium to incorporate ion channels for specific sensing applications. We present that a single layer of graphene field-effect transistor is sensitive to different KCl concentrations and pH levels by observing the shift of graphene's Dirac point. Then the supported lipid bilayers are deposited on graphene surface to form a barrier for different KCl concentrations and pH solutions. Finally, the graphene-supported lipid bilayer biosensors are assembled with alamethicin and gramicidin A (gA) channels to study the single ion channel activity. This is the first time single ion channel activity of alamethicin and gramicidin A channels has been presented in graphene field-effect transistors with different applied voltages.

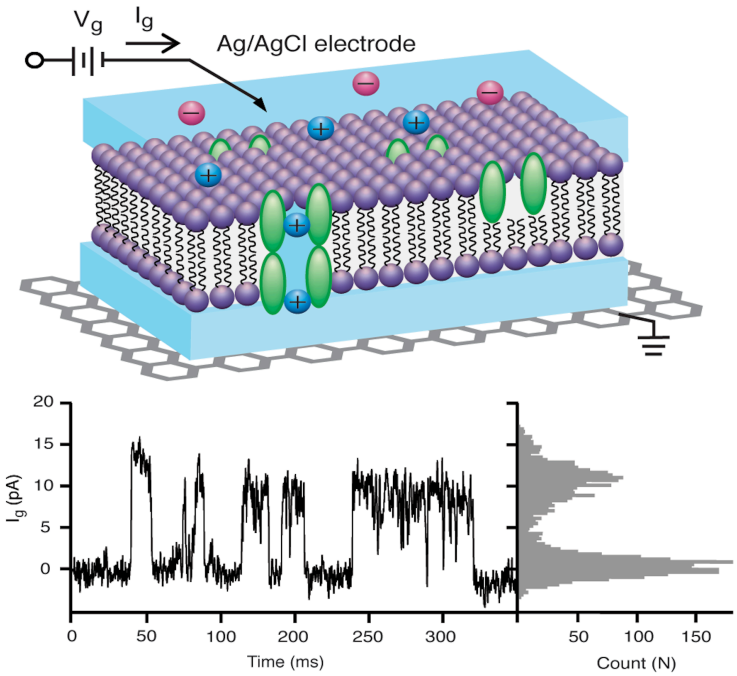

Figure 1.2. Schematic diagram of SLBs with gA on graphene surface for ion channel activity detection, current trace for ion channel activity of gA at V_g=100 mV in 1 M CsCl, and histogram of current trace.

In third work, we focus on the electrostatic gating effect of charged species in direct contact with the graphene surface, since most chemical and biological molecules in the aqueous solution will bear some charges. In order to study the exact nature of this interaction, we employed the positive and negative charged polymer electrolye multilayers polyallylamine hydrochloride (PAH) and sodium polystyrenesulfonate (PSS) to mimic charged molecules on graphene's surface (Figure 1). These polyelectrolyte multilayers (PEMs) PEMs are prepared by the layer-by-layer deposition of polyanions and polycations from aqueous solutions. With this technique, polyanion/ polycation complexes are formed with charge reversal after each successive layer. Using these species, we also can control and predict the shift of the graphene's Dirac point by the adsorption of different polymer layers, and effectively change the graphene from p – type to n-type at will. The Dirac point of graphene displays periodic behavior during sequential addition of positively and negatively charged polymers on the graphene surface. A simple electrostatic model is applied to interpret these results.

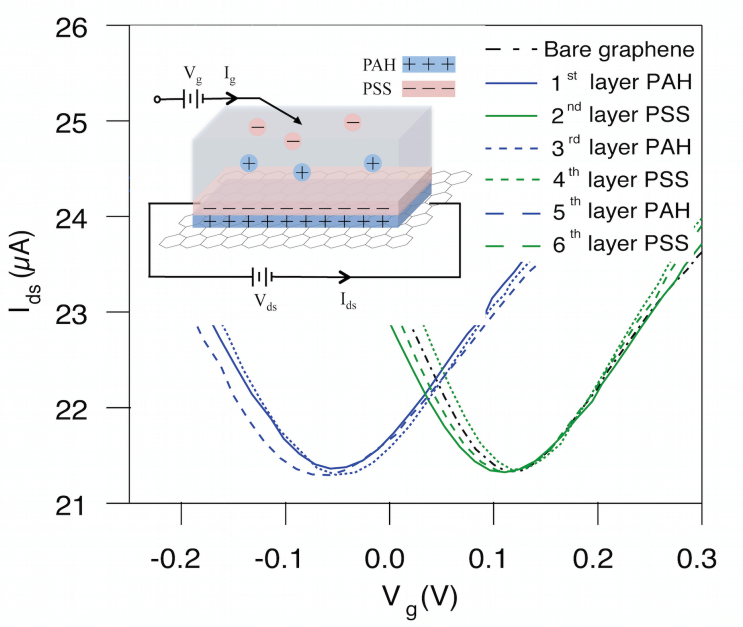

Figure 1.3. Schematic illustration of polyelectrolyte multilayers PAH and PSS deposited on the surface of single layer graphene as well as transfer characteristics of graphene FET devices as a function of # of PAH/PSS multilayers.

CHAPTER TWO

A LARGE-AREA AND CONTAMINATION-FREE GRAPHENE TRANSISTOR FOR LIQUID-GATED SENSING APPLICATIONS

2.1. INTRODUCTION

Graphene, an atom-thick layer of sp^2-bonded hexagonal carbon[10,11] due to its uniquely two-dimensional surface is an advanced candidate for chemical and biological sensors[12,13]. Recently, several graphene synthesis methods have been developed, such as chemical vapor deposition (CVD) on metal substrate Ni[14] and Cu[15]. Chemical vapor deposition has been demonstrated as a reliable method for self-limited growth of single-layer graphene on copper foil[6]. However, the sensor fabrication and graphene transfer usually involve the use of photoresists and polymethylmethacrylate (PMMA) on graphene surface, causing contamination[16] and n-type doping[17]. Although recent works have shown that using thermal treatment about 300~400 ˚C in H_2/Ar atmosphere[7] or in high-vacuum[18,19] can remove most of photoresists and PMMA, the remaining residues could still hamper sensor applications. Annealing at high temperature may lead to heavy hole doping and mobility degradation of graphene[20]. Moreover, high temperature, post transfer anneals are not compatible with polymer substrates such as polydimethylsiloxane (PDMS), widely used in microfluidics and sensing applications.

Although the transfer of graphene using PDMS has already been reported in existing literatures[21-28], the PDMS is used as stamp to print graphene on the different substrates like SiO_2 wafer. There is no graphene field-effect transistors (FETs) made directly on PDMS substrates for sensing applications. Whereas transfer printing of graphene can provide a contamination-free method for device fabrication, it may only work on multilayer and small area graphene with 100 μm for the channel length of graphene transistors. Because the transfer printing method is totally dependent on the surface adhesion between the graphene film and the target substrate, it is difficult to transfer large area monolayer graphene. Hence, these problems may impede the applications of graphene-based sensors.

2.2. FABRICATION OF DEVICE

2.2.1. FABRICATION PROCESS

Figure 2.1. shows a schematic illustration of transfer process. We physically attached a PDMS block on a commercial CVD-grown single layer graphene on copper foil (ACS Material). Then PDMS/graphene/foil block was floated on the surface of 0.05 g/ml ammonium persulfate solution (Aldrich, 98%) to etch copper foil. After the copper was etched, the PDMS/graphene block was rinsed with deionized water several times. Then the second layer of PDMS with open well was employed to hold electrolyte solution. Finally, source and drain electrodes were directly deposited by silver conductive paint[29].

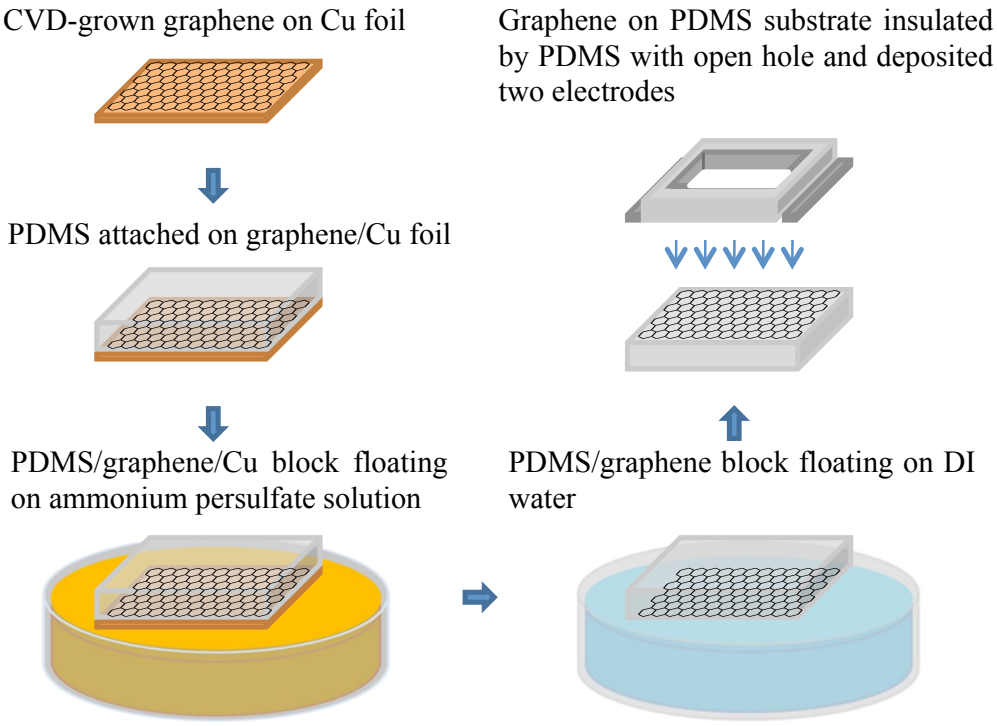

Figure 2.1. Schematic illustration of graphene film in transfer, etch, and fabrication on PDMS substrate.

2.2.2. MONOLAYER GRAPHENE FET DEVICE

This device is made by direct transfer process in figure 2.1. The top layer PDMS with the 1 cm × 0.3 cm hole is used to hold electrolyte solution. The liquid gate voltage is applied through a Ag/AgCl electrode to electrolyte solution. Beside the top layer PDMS are two source and drain electrodes which are deposited by silver conductive paint. The graphene film is transparent and under the top layer PDMS and the two electrodes. The size of graphene is 1 cm × 1 cm. The distance between two electrodes is 0.6 cm.

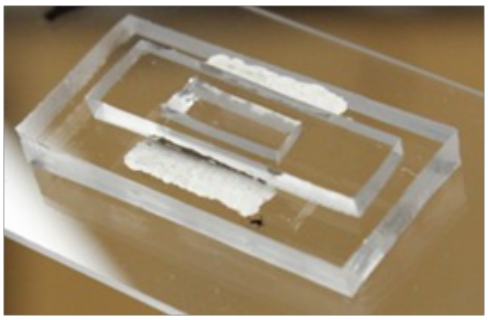

Figure 2.2. Optical image of monolayer graphene FET on PDMS substrate.

2.3. CHARACTERIZATION

2.3.1. OPTICAL, RAMAN SPECTRUM, AFM AND SEM IMAGES OF GRAPHENE

Figure 2.3.(a) is an optical image of monolayer graphene with size 1 cm × 1 cm on a PDMS substrate. Figure 2.3.(b) shows Raman spectrum (532 nm laser wavelength) of graphene transfer-printed from PDMS onto SiO_2 /Si wafer. Because PDMS substrate will show some noise peaks on the Raman spectrum[29], we decide to transfer and print graphene onto the SiO2 /Si wafer for Raman investigation. The G and 2D peaks of graphene film are positioned at 1566 cm^{-1} and 2675 cm^{-1}, respectively. The ratio of the integrated intensity of G band to 2D band is 0.3, which suggests the graphene film to be monolayer[30]. Also, a negligible defect-related D band is at 1330 cm^{-1}, which indicates the defects caused during transfer printing from PDMS to SiO2 /Si wafer. We also used atomic force microscopy to examine the thickness of the graphene film. The thickness of our graphene film is about 0.5 nm in our previous work[31]. From these results, the film on the PDMS substrate shows a high quality monolayer graphene[32]. Figure 2.3.(c) presents a typical AFM image of single layer graphene surface on PDMS substrate. There are some

wrinkles in the AFM image. Those wrinkles are formed during the cooling step in the CVD-growth process due to the difference of thermal coefficients between the graphene film and copper foil. Except those wrinkles, no resides are observed, which indicates the graphene surface is very clean. Figure 2.3.(d) shows a scanning electron microscopy (SEM) image of single layer graphene on the PDMS substrate. Then sample is observed directly under scanning electron microscopy without any coating. Graphene sheet is complete over the PDMS substrate.

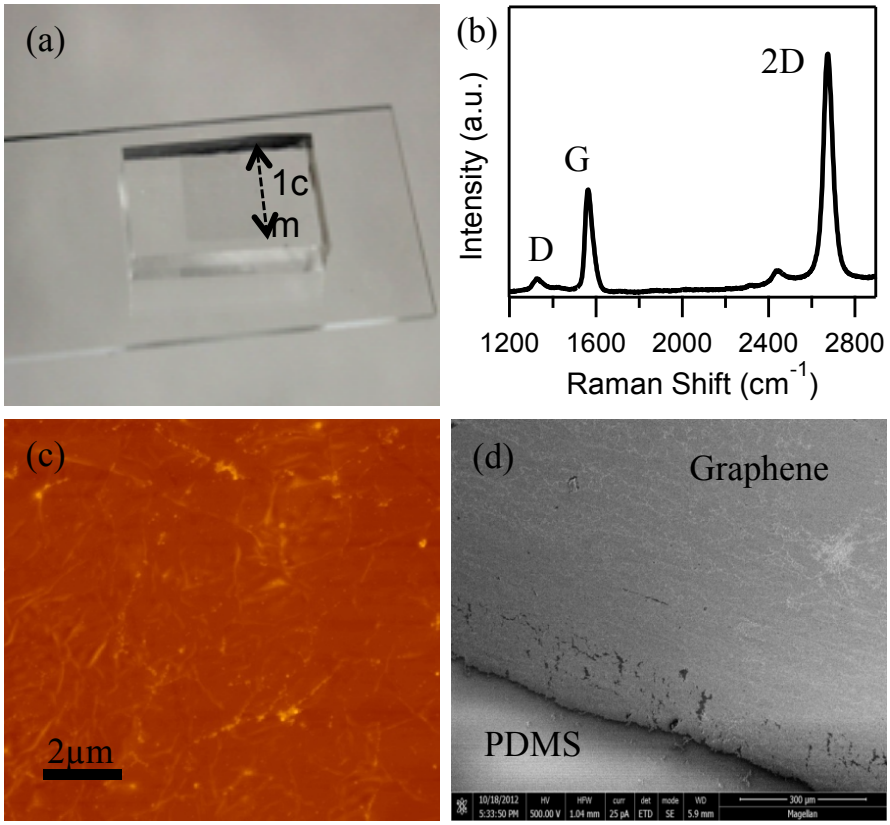

Figure 2.3. (a) Optical image of monolayer graphene on PDMS substrate. (b) Raman spectrum of monolayer graphene transfer-printed from PDMS to SiO_2/Si substrate. (c) AFM image of monolayer graphene surface on PDMS substrate. (d) SEM image of monolayer graphene border on PDMS substrate.

2.3.2. RAMAN SPECTRA OF GRAPHENE ON PDMS

After graphene is transferred onto PDMS, the sample is investigated by Raman spectroscopy. The blue curve is showing Raman spectrum of monolayer graphene on PDMS. The 2D and G peaks are observed as single layer graphene. The D peak is not present in the curve. This indicates transfer to the PDMS substrate does not generate any defects in the graphene film. The other noise peaks are not from the graphene film. They are generated by the PDMS substrate which is showed in the red curve. In order to avoid those noise peaks from PDMS, we transferred graphene film from PDMS to SiO_2/Si substrate for Raman characterization. The Raman spectrum of the graphene film is showed in figure 2.4.

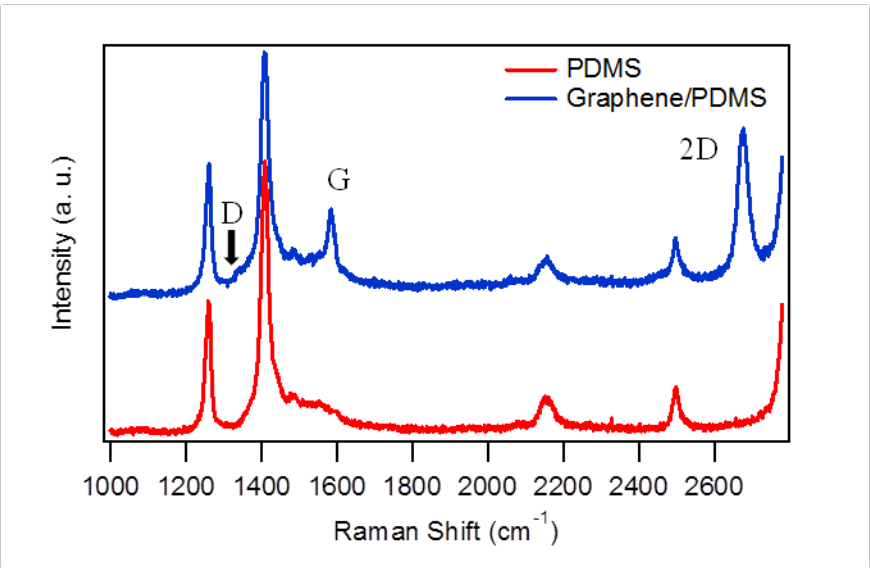

Figure 2.4. Raman spectra of PDMS and graphene/PDMS.

2.3.3. LEAKAGE CURRENT OF GRAPHENE FET

During the liquid gating measurement, we also examined the current from graphene device to solution. Figure 2.5.(a) shows the schematic illustration of graphene device. I_g is gate current which is current flowing from graphene to Ag/AgCl reference electrode. Figure 2.5.(b) presents this gate current *vs.* gate voltage. The gate current is less than 15 nA at the maximum applied gate voltage. This indicates that top layer PDMS can effectively insulate the electrolyte with two source and drain electrodes.

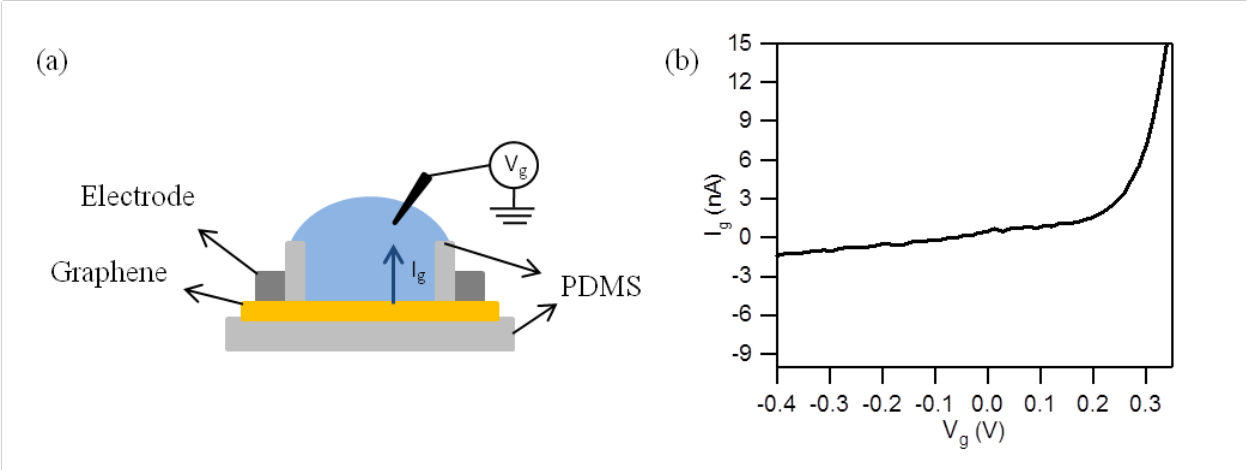

Figure 2.5. (a) Schematic illustration of graphene device for investigation of gate current. (b) The liquid gate current *vs.* liquid gate voltage characteristics of graphene FET in 0.1 mM phosphate buffer at pH 7 with 100 mM KCl.

2.3.4. CONTACT RESISTANCE OF SILVER PASTE ON GRAPHENE SHEET

For the contact resistance between silver paste and graphene sheet, the device is examined by two-electrode measurement. Figure 2.6.(a) is I_{ds} *vs.* V_{ds} measurements of graphene on PDMS with different channel length from 1 mm to 5mm. From this figure, we can get the total contact resistance in response to different channel length. By drawing figure total resistance *vs.* channel length in figure 2.6.(b), we can figure out the fitting line and the equation. From this equation, we can know that the contact resistance is about 917 Ω.

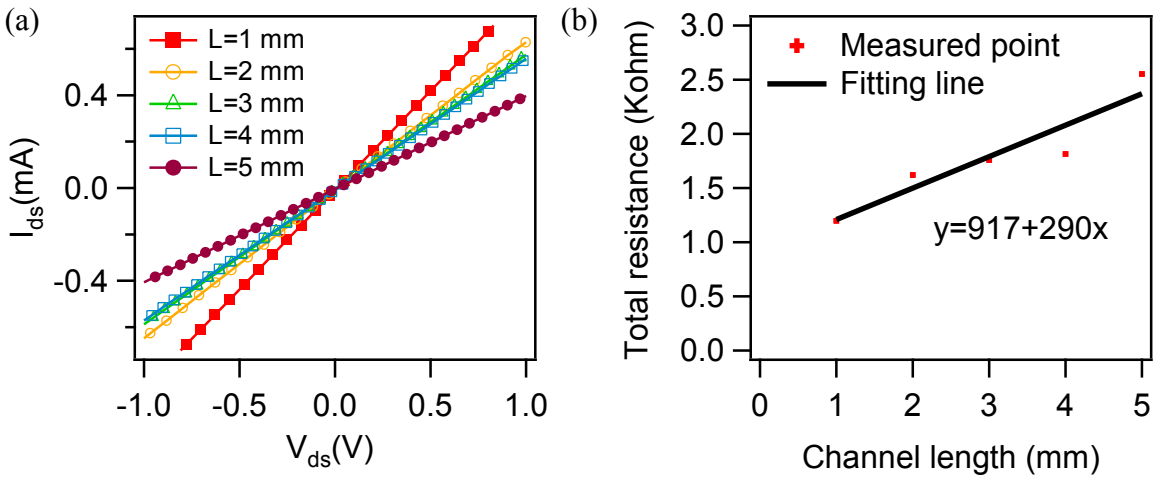

Figure 2.6. (a) I_{ds} *vs.* V_{ds} measurements of graphene on PDMS with different channel length. The two electrodes are painted by silver paste. (b) The device's total resistance *vs.* channel length.

2.3.5. AFM TOPOGRAPHIC IMAGES OF PMMA/GRAPHENE FILM

In order to investigate graphene surface by PMMA transfer method, graphene/copper film was spin-coated by a 300 nm thickness of PMMA. After copper foil was etched, the PMMA/graphene film was transferred onto Si wafer and soaked in acetone for overnight. Figure

2.7.(a) is AFM topographic image of PMMA/graphene film after cleaned by acetone. The scan size is 10 μm x 10 μm and black bar is 2 μm. The graphene surface is filled with PMMA residues. That means the acetone bath cannot effectively eliminate the PMMA. Figure 2.7.(b) is AFM line scan from figure 2.7.(a). The highest PMMA residue is 53 nm. Then this sample was annealed in forming gas (Ar 95% / H2 5%) at 400 ˚C for 3 hours. Figure 2.7.(c) is AFM topographic image of PMMA/graphene film annealed in forming gas. Most of PMMA residues are eliminated. But some 1 ~ 2 μm width and 50 nm height PMMA residues are left which are showed in figure 2.7.(d). Our work avoids all of these contamination issues as discussed in the main text.

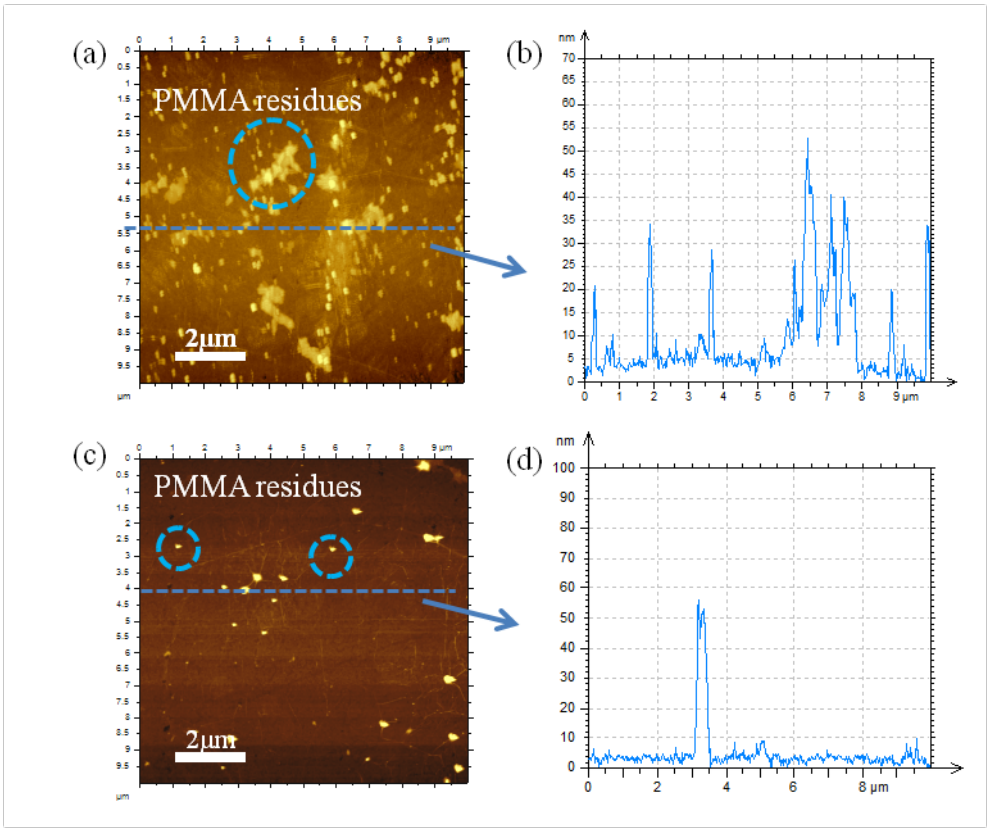

Figure 2.7. (a) AFM topographic image of PMMA/graphene film soaked in acetone bath for overnight. (b) AFM line scan from figure 2.7.(a). (c) AFM topographic image of

PMMA/graphene film annealed in forming gas (Ar 95% / H2 5%) at 400 ˚C. (d) AFM line scan from figure 2.7.(c).

2.3.6. AFM IMAGE OF SINGLE LAYER GRAPHENE

Atomic force microscopy is employed to determine the number of the layer of CVD-grown graphene. The sample is prepared by spin-coating a layer of PMMA on graphene/copper film. After copper foil is etched, the PMMA/graphene film is transferred onto Si wafer. The PMMA is eliminated by acetone overnight and annealing in forming gas (Ar 95%/ H2 5%) at 400 ˚C for 3 hours. The thickness of this transferred graphene is about 0.5 nm. This indicates the CVD-grown graphene film is single layer. More detail and image are showed in our previous work[31].

2.3. DISCUSSION

2.3.1. EFFECTS OF GRAPHENE WITH DIFFERENT ETCHING SOLUTION

Figure 2.8.(a) presents the device layout of liquid gated graphene transistor. The source and drain electrodes were deposited by silver paint, and PDMS with a hole was used to insulate the ionic solution from the electrodes. The graphene film was gated through a Ag/AgCl reference electrode in the ion solution. Figure 2.8.(b) shows the liquid-gated ambipolar filed-effect characteristics of the graphene transistor (I_{ds} *vs.* V_g , V_{ds}= 100 mV) in 100 mM KCl solution. The transfer characteristics present a V-shaped p- to n-type transition. The mobility of the device can be calculated from the equation l. $(L/WC_gV_d)(\Delta I_d/\Delta V_g)$[8], where L and W are the channel length

0.3 cm and width. 0.6 cm, and Cg capacitance of graphene is 57 nF cm^2. The liquid-gated hole and electron mobility are 2053 cm^2 /(V s) and 1429 cm^2 /(V s), respectively. The leakage current is less than 15 nA in the range of applied gate voltage[29]. The contact resistance between silver paste and graphene is about 917Ω[29]. Although the contact resistance can affect the device total electrical characteristics if it is comparable to the channel resistance such as in short channel devices[33], in our case the contact resistance is much less than the channel resistance (we have a very long channel) and so does not affect the extrapolated mobility calculation. More quantitatively, it is well known in the device physics field that if the transconductance–contact resistance product is less than one (which is the case for our measurements), it does not affect the total (measured) transconductance.

In order to understand the effect of different etching solution on graphene's Dirac point during the transfer process, the copper foil is etched by three different solutions, $FeCl_3$ (0.05 g/ml), $Fe(NO_3)_3$ (0.05 g/ml), and $(NH_4)_2S_2O_8$ (0.05 g/ml) for 5h. Because of the ambipolar characteristics of graphene, we can see the field-effect response V-shaped which is both hole and electron conductance in the graphene FETs. For a perfect and contamination-free graphene device, the Dirac point should close to zero. When the graphene surface has adsorbed any chemicals, the Diract point of graphene will shift to positive or negative gate voltage. By observing the shift of the Dirac point, we can determine the change of graphene surface. Figure 2.8.(c) is drain-source current variation of graphene FETs etched by $FeCl_3$ (red), $Fe(NO_3)_3$ (blue), and $(NH_4)_2S_2O_8$ (green) as a function of the gate voltage in 0.1mM phosphate buffer at pH 7 with 100 mM KCl and 100 mV drain source voltage. A linear blue curve is observed across the liquid gate voltage range. This indicates that the graphene sheet adsorbs the NO_3^- ions during the etching process. This n-type doping will make the Fermi level of graphene shift to valence

band. In order to see the Dirac point, the more positive gate voltage should be applied. It is difficult to get rid of this contamination by rinsing with deionized water even for a longer time. Graphene films which are etched by $FeCl_3$ and $(NH_4)_2S_2O_8$ show V-shaped I_{ds}-V_g curves (red and green curves, respectively). However, the Dirac point of the red curve is around 0.18 V. This shows that the graphene film has minor n-type doping contamination by $FeCl_3$ etching solution. The reason is the adsorption of Cl^- ions on the graphene sheet during the etching process. This negative ions doping will shift the Fermi level of graphene to valence band. Then the Dirac point will shift to more positive gate voltage. We do not see any improvement upon rinse with deionized water for a longer time. Finally, the green curve has Dirac point around 0.02 V. This indicates graphene film etched by $(NH_4)_2S_2O_8$ has less doping contamination.

In figure 2.8.(d), we show drain-source current variation of graphene FETs etched by different concentrations of solution $(NH_4)_2S_2O_8$ (0.1 g/ml red, 0.05 g/ml blue, and 0.02 g/ml green) as function of the gate voltage in 0.1mM phosphate buffer at pH 7 with 100 mM KCl and 100 mV drain source voltage. Three different concentrations all show V-shapes in the range of applied gate voltage. Only the green curve's Dirac point has right shift around 0.2 V. This shows 0.02 g/ml $(NH_4)_2S_2O_8$ concentration will cause minor n-type doping contamination on graphene surface, due to the fact that the lower concentration needs a longer etching time to get rid of the copper foil. Longer etching time may lead to some negative ions adsorption on graphene film. Therefore, the Dirac point of graphene has positive shift. In the higher concentration 0.1 g/ml and 0.05 g/ml, both of them have Dirac point around 0.04 V and 0.02 V, respectively. Because of high concentration, they can quickly etch away copper foil without causing n-type doping in the graphene film. However, while comparing to the hole and electron mobility, blue curve (0.05 g/ml) has hole and electron mobility 1922 cm^2 /(V s) and 1375 cm^2 /(V s), which are higher than

red curve's (0.1 g/ml) hole and electron mobility 1351 cm^2 /(V s) and 1024 cm^2 /(V s), respectively. Since higher $(NH_4)_2S_2O_8$ concentration (0.1 g/ml) has more rapid reaction during etching process, this will cause some degradation of the graphene quality. We conclude the etching solution $(NH_4)_2S_2O_8$ (0.05 g/ml) is the optimize concentration for our device fabrication without any doping contamination and mobility degradation.

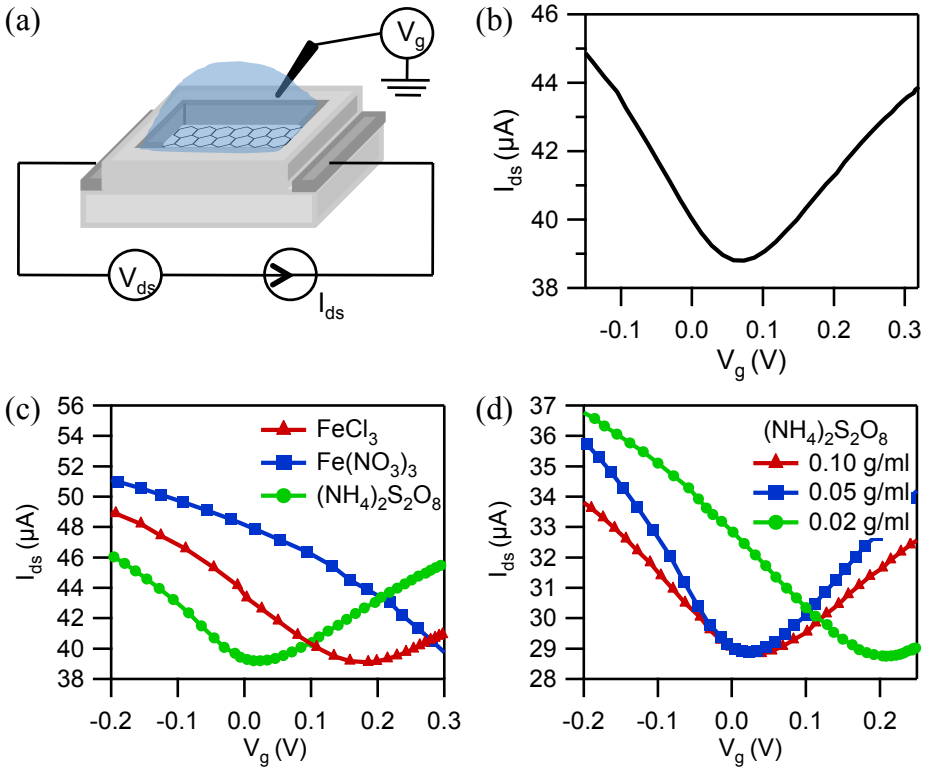

Figure 2.8. (a) Schematic illustration of single layer graphene field-effect transistor on PDMS. substrate. (b) The drain-source current *vs.* liquid gate voltage characteristics of single layer graphene FETs on PDMS substrate in 0.1 mM phosphate buffer at pH 7 with 100 mM KCl and V_{ds}= 0.1 V. (c) The effect of graphene FETs' transfer curves in different etching solution $FeCl_3$,

$Fe(NO_3)_3$, and $(NH_4)_2S_2O_8$. (d) The effect of graphene FETs' transfer curves in different concentration of $(NH_4)_2S_2O_8$ (0.1 g/ml, 0.05 g/ml, and 0.02 g/ml).

2.3.2. EFFECTS OF GRAPHENE WITH DIFFERENT KCL CONCENTRATION AND PH VALUES

In order to demonstrate the sensing applications of our devices, we investigated our devices with liquid gating in different KCl concentrations and pH values. Figure 2.9.(a) shows drain-source current as function of gate voltage in different KCl concentrations. The I_{ds}-V_g curve is shifted to left while the ionic strength is increased. This indicates an electrostatic gating effect happens. The electrostatic gating effect is generated by surface potential at the graphene-liquid interface. When the negative surface charge which is screened by ions attracts mobile positive charges to the graphene-liquid interface, the negative surface potential is formed. These positive charges are both positive charges (holes) in the graphene and positive ions in the electrical double layer in solution. At higher ionic strength, the electrical double layer is compressed which will decrease the negative surface potential. Then the lesser positive gate voltage is required to compensate this negative surface potential. Therefore, the positive shift of the Dirac point becomes smaller. This result is in agreement with previous studies[34-36]. Figure 2.9.(b) is V_{shift} of Figure 2.9.(a) as a function of KCl concentration with respect to 1 M KCl. In the curve, the V_{shift} is linear to log ([KCl]) over the 3 orders of magnitude concentration change.

Figure 2.9.(c) shows drain-source current as function of gate voltage in different pH values. An increase in pH from pH 4 to pH 10 causes s shift toward more positive V_g. At higher pH,

there is more adsorption of OH^- ions on graphene surface. Then the negative surface potential becomes larger. The higher positive gate voltage is applied to compensate this negative surface potential. Thus, the Dirac point of graphene will shift to more positive gate voltage. This result also observed in other reports[12,13]. Figure 2.9.(d) is V_{shift} of figure 2.9.(c) as a function of pH value with respect to pH 4. This curve also shows the V_{shift} is linear to change of pH value. Our work is different than previous studies[12,13,25–27] from using direct transfer graphene FETs device without any contamination of photoresists and PMMA. By operating these two experiments, our graphene FET shows highly potential for chemical and biological sensing applications.

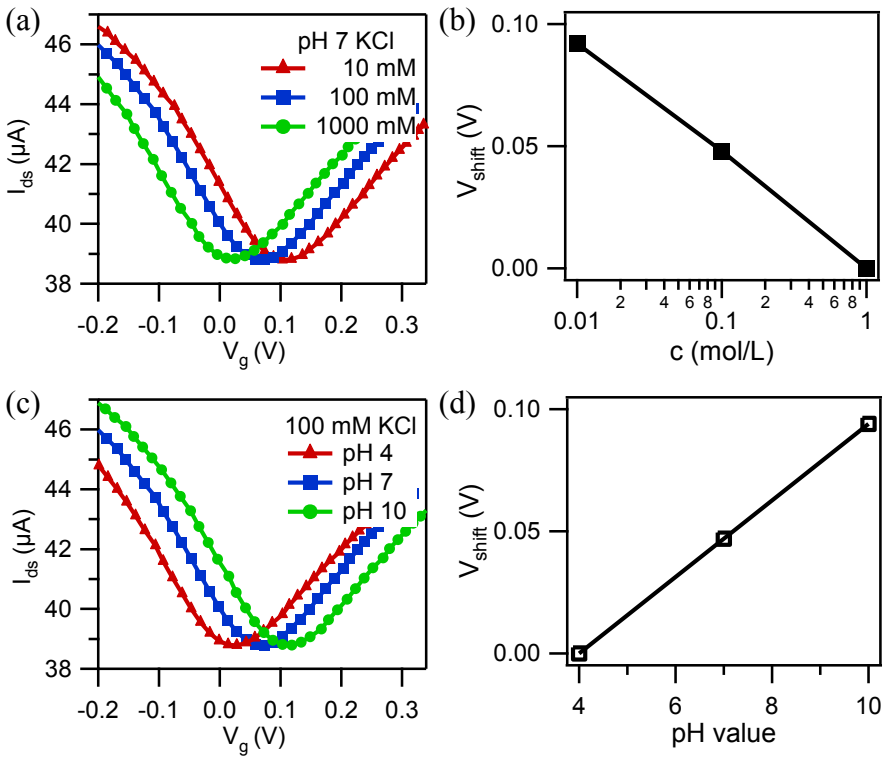

Figure 2.9. (a) The drain-source current *vs.* liquid gate voltage characteristics of graphene FET in

0.1 mM phosphate buffer at pH 7 with 10 mM KCl (red), 100 mM KCl (blue), and 1 M KCl (green). (b) Shift of the I_{ds}-V_g curves in (a), V_{shift} with respect to the 1M KCl, as a function of the KCl concentration. (c) The drain-source current *vs.* liquid gate voltage characteristic of graphene FET in 0.1 mM phosphate buffer with 100 mM KCl at pH 4 (red), pH 7 (blue), and pH 10 (green). (d) Shift of the I_{ds}-V_g curves in (c), V_{shift} with respect to the pH 4, as a function of the pH value.

2.4. CONCLUSION

In conclusion, we have demonstrated a simple, low-cost, large area, and contamination-free monolayer graphene field-effect transistor on PDMS substrates for liquid-gated sensing applications. This device not only avoids the contamination of photoresists and PMMA but also prevents the mobility degradation of annealing process on the graphene film. Therefore, our graphene field-effect transistors present a large area and contamination-free clean monolayer graphene surface. This clean graphene surface FET can provide a platform to study the effects of many different chemical and biological materials with monolayer graphene by liquid-gated ambipolar characteristics. In addition, we investigated the effects of graphene's Dirac point in different etching solutions and concentrations on graphene film. We also demonstrated the liquid-gated sensing applications for different KCl concentrations and pH values. We believe that our devices have substantial potential for chemical and biological liquid-gated sensor applications.

CHAPTER THREE

CHARGING THE QUANTUM CAPACITANCE OF GRAPHENE WITH A SINGLE BIOLOGICAL ION CHANNEL

3.1. INTRODUCTION

Supported lipid bilayers (SLBs) have risen as a robust alternative to the traditional and fragile black membranes for studying ion channel electrophysiology, a key component in biological signaling pathways to passively and selectively transport ions across the impermeable cell membrane. The traditional approach of forming a lipid bilayer across a microscale aperture is extremely flimsy, requiring high level of expertise, which limits throughput. In contrast, SLBs are more robust, easy to make, and potentially applicable toward high throughput[37-40]. As an atomically thin 2d material, graphene provides an attractive choice as the electrode for such electrophysiology studies, as it adds many additional properties that may be exploited for novel interactions with ion channels. For example, the in plane conductance of graphene is extremely sensitive to the environment, yielding proposals for applications in resistive biosensing[41]. An additional method of excitation of graphene is capacitive rather than resistive biosensing, which to date has not been exploited, in spite of the known extreme quantum limit of graphene[42], where the capacitance is dominated by the finite energy required to add charge to a quantum system, called the quantum capacitance. In order to explore and exploit the unique properties of reduced dimensional materials (such as graphene) for novel applications in electrophysiology, it is necessary first to develop a fundamental understanding of the basics of the interaction between 2d materials such as graphene, lipid bilayers, and ion channels and the effects of the interactions on charge transport in these systems.

In this study, we integrate a supported lipid bilayer (SLB) onto a graphene electrode, and demonstrate electrical sensing of the opening and closing of individual ion channels gramicidin A (gA) and alamethicin in the SLBs. The SLB forms an insulating barrier as confirmed by

several techniques. The Dirac point of the graphene FETs is not affected by changes in the solution pH or KCl concentration after it is covered by SLBs. By careful measurement and analysis of the appropriate circuit elements in an equivalent circuit model, we confirm that the ion channel current in our setup directly charges the quantum capacitance of the graphene. This is a qualitatively different type of interaction than traditional SLBs with metal electrodes, since metal electrodes do not exhibit quantum capacitance effects. Although we previously showed single ion channel activity with 1d devices[43-45], this is the first time the activity of single ion channels (including gA and alamethicin) has been presented in 2d (specifically graphene) electronic devices.

In this work, the graphene acts as an electrode on one side of the SLB, and current changes observed are due purely to changes in the membrane permeability induced by the opening and closing of ion channels, similar to the case where metal electrodes are used for the same purpose. Qualitatively, the capacitance that is charged is different in this case (the quantum capacitance), as opposed to a metal electrodes, in which only the double layer capacitance is charged. As graphene is a new material with many possible opportunities for heterogeneous integration in complex systems, there are many potential advantages of using graphene for this purpose, for example in printed and flexible electronics on biocompatible polymers for *in-vivo* electrophysiology sensing of neurons (e.g. as a component of the US government BRAIN initiative[46,47]), cardiomyocites, pancreatic beta cells, and other electrophysiologically active cells. The measurement of single ion channels represents the ultimate in sensitivity for such an *in-vivo* measurement. Furthermore (in contrast to metal electrodes), as the graphene layer is optically transparent (and can even be optically active[41]), it provides for an opportunity to integrate electrophysiology with optics (both external as well as optically active membrane proteins such

as the rhodopsins in both actuation and sensing mode), an exciting frontier area in optogenetics and single ion channel sensing[48]. Finally, as graphene is an active material, this is an important step towards integrating in-plane current sensing of ion channel currents with 2d and 1d[43-45] nanoelectronic devices. Thus, this work should be seen as a first step towards integration of nanoelectronics with electrophysiology at the single ion channel level.

While all of these exciting applications are yet to be demonstrated, the novel aspect of this work is the first demonstration of the charging of the quantum capacitance (a nano-electronic concept) with the ionic currents flowing through biological nanopore (an electrophysiology concept). This general approach thus presents novel and qualitatively new ways that ion channel electrophysiology can be integrated with the quantum properties of reduced dimensional systems such as graphene, paving the way for a new class of devices to probe and assay biological process using the unique quantum and electrical properties of a wide range of nanotechnology based systems where the reduced dimensionality plays a key role.

3.2. METHODS

3.2.1. CHEMICALS

Iron(III) nitrate nonahydrate (ACS reagent, ≥98%), potassium chloride (bioXtra, ≥99%), cesium chloride (optical grade, ≥99.5%), phosphate buffer solution and alamethicin were purchased from Sigma Aldrich. Gramicidin A was from Enzo Life Sciences. Polydimethysiloxane (PDMS) was made by sylgard 184 silicone elastomer kit. 1,2-diphytanoyl-*sn*-glycero-3-phosphocholine (DPhPC) in chloroform was obtained from Avanti Polar Lipids.

1,2-Dihexadecanoyl-*sn*-Glycero-3-Phosphoethanolamine, Triethylammonium Salt (rhodamine DHPE) was from Life Technologies. CVD-grown single layer of graphene on copper foil was obtained from ACS Material.

3.2.2. FABRICATION AND MEASUREMENT OF GRAPHENE FETS

The graphene device was transferred and fabricated by polydimethysiloxane (PDMS) block as described in our previous publication[49]. The second layer of PDMS with a 1 mm × 1 mm well was attached on top of the graphene to insulate the solution from the two electrodes for the liquid-gating effect and ion channel measurements. The electrolyte is a 0.1 mM phosphate buffer at pH 7 in 100 mM KCl. The gate voltage is applied by a Ag/AgCl reference electrode. The drain-source current *vs.* gate voltage was measured by Agilent 34401A multimeter.

3.2.3. FORMATION OF SUPPORTED LIPID BILAYERS WITH ION CHANNELS ALAMETHICIN AND GRAMICIDIN A ON GRAPHENE DEVICES

The supported lipid bilayers (SLBs) were prepared by evaporating 160 μl of DPhPC (25mg/ml) in chloroform under nitrogen flow. After the dried lipid films were obtained, 5 ml of 10mM phosphate buffer was added to rehydrate at 55 ˚C for 1h. Then the lipid suspension was sonicated for 1h to form small unilamellar vesicles (SUVs). In order to get homogeneous SUVs, the suspension was filtered by a 0.2 μm nylon filter. For the deposition of the SLBs on graphene, the lipid suspension was dropped on the graphene device with PDMS well as described above.

This was followed by incubation of lipid vesicles on the graphene devices for 3 h at 60 ˚C to form supported lipid bilayers on the graphene surface. Then the device was cooled for 30 min. The unbounded lipid bilayers were removed by rising with distilled water for 10 times. As in ref.[15], we found the best results when the graphene device was soaked by distilled water overnight prior to deposit the SLBs on graphene surface. In order to prevent disintegration of SLBs, the solution must be maintained on the devices all the time. For the fluorescence study, 1 mM of fluorescent dye solution (rhodamine DHPE) was added to label lipids for two hours before evaporation of chloroform. For the study of ion channel alamethicin, a solution of 10μg/ml of alamethicin in 100 mM KCl was added into the graphene-supported lipid bilayers devices. For the formation of ion channel gA with SLBs, 0.1 mM of gA was mixed with DPhPC suspension in chloroform for two hours before solvent evaporation. If desired, the lipid bilayer can be dissolved by adding detergents.

3.2.4. EQUIPMENT SET UP FOR CHARACTERIZATION

For Raman spectroscopy, a 532 nm excitation laser and a 50X objective lens were used for graphene film investigation. The graphene film was prepared by transfer-printing from PDMS onto SiO_2/Si substrate in order to reduce the noise peaks which are generated by the PDMS substrate. For observing SLBs, the fluorescent dyes (rhodamine DHPE) were mixed with DPhPC at 0.1% molar ratio. Images were obtained using an inverted microscope (Olympus IX-71) with a digital monochrome CCD camera.

3.2.5. EQUIPMENT SET UP FOR ION CHANNEL ACTIVITY MEASUREMENT

Ion channel activity was measured by a patch clamp amplifier (Axopatch 200B, Axon Instruments) which was placed on a vibration isolation table with a Faraday cage shield. The electrolyte voltage was applied by a Ag/AgCl electrode and ground was connected to the source terminal of the graphene device, with the drain terminal floating. The signal was acquired and digitized by Digidata 1440A (Axon Instrument) and passed through a 1 kHz filter and digitized at a 10 kHz sampling rate. Data collection was performed by electrophysiology software (pClamp10).

3.3. CHARACTERIZATION

3.3.1. FLUORESCENCE IMAGES OF LIPID BILAYER

The quality of lipid bilayer is characterized by fluorescence images. Figure 3.1.(a) presents good quality of lipid bilayer on graphene surface. Figure 3.2.(b) is bad quality of lipid bilayer on graphene surface.

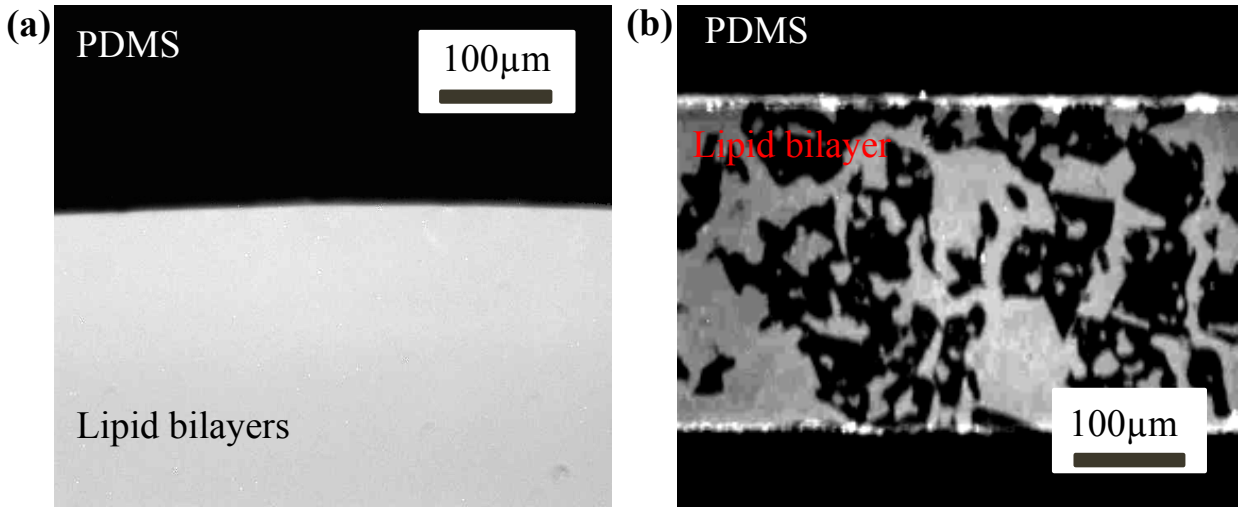

Figure 3.1. Fluorescence images of lipid bilayer on graphene surface (a) good quality and (b) bad quality.

3.3.2. BILAYER DETERMINATION BY FLUORESCENCE QUENCHING

We developed a fluorescence based method to distinguish between bilayers, mono-bilayers and multi-bilayers. QSY-7 amine (Invitrogen, Q-10464) was used to determine whether an artificial lipid layer consists of a bilayer or otherwise[50]. The working principle is that QSY-7 amine can quench, via FRET, the fluorescence of the lipid dye reporter TexasRed DHPE (Invitrogen #T1395MP) embedded into the lipid layer. If a supported lipid bilayer is truly a bilayer, only the top layer is accessible to QSY-7 amine and therefore adding the quencher will reduce roughly half of the total fluorescence intensity. Similarly, the reduction will be less if the lipid layer is a multilayer. In our test, we fabricated SLBs on graphene as described in the method but included 0.5% mol of TexasRed DHPE for fluorescence measurement. We chose to

image a field of view equivalent to 420x220 µm at the center of the graphene device to represent the quality of the deposited bilayer (Figure 3.2.(a)).

The images were taken with an inverted IX71 fluorescence microscope equipped with a broadband excitation lamp and a TRITC filter. The fluorescence intensity is measured and false colored red with Image J. After taking initial images, 2 µL of 48 uM QSY-7 amine was added to the bath solution and images were retaken for the same field of view after 2 min incubation (Figure 3.2.(b)). Of all the devices we tested, 30% showed approximately 50% decrease in fluorescence intensity, indicating the formation of a true lipid bilayer (Figure 3.2.(c)). Once we determined the bilayer nature of our supported bilayer, we proceeded to capacitance measurement of the same device.

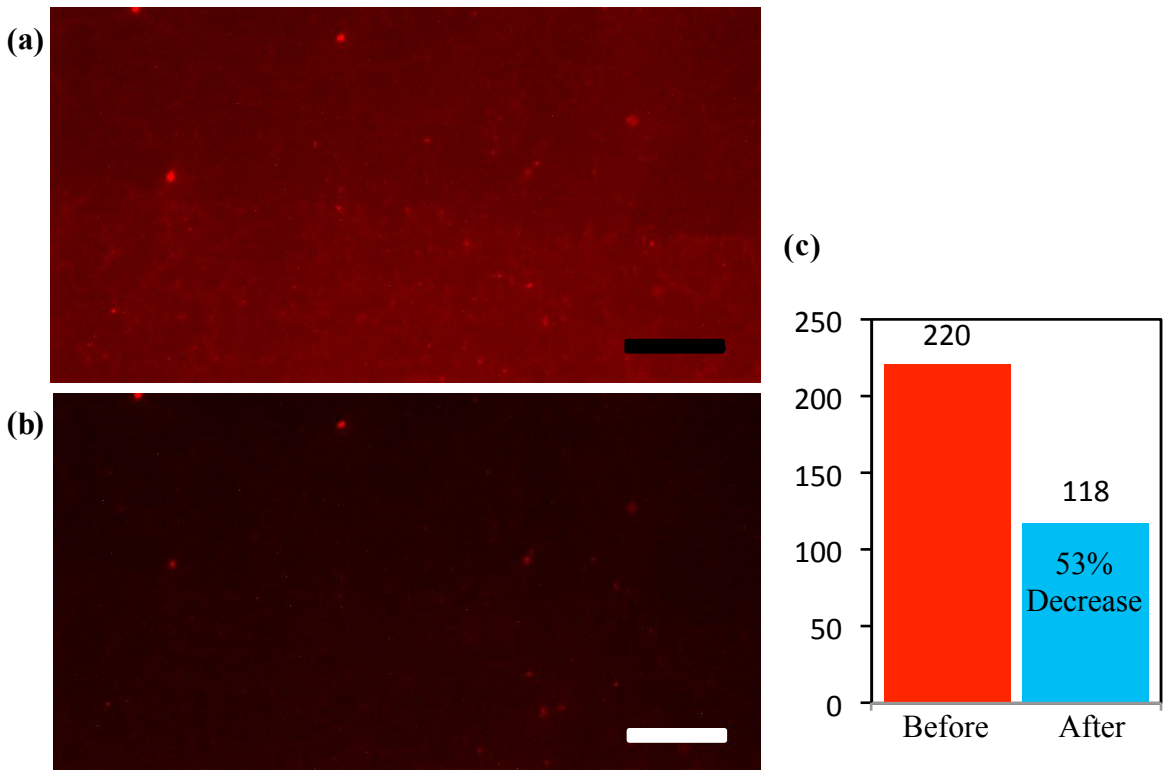

Figure 3.2. Images of the same field of view (a) before and (b) after adding QSY-7 amine. Scale bars are 50 μm. (c) Measured fluorescence intensity of the field of view before and after the addition of QSY-7 amine.

3.3.3. FLUORESCENCE RECOVERY AFTER PHOTOBLEACHING (FRAP) OF SLBS ON GRAPHENE SURFACE

For the fluorescence recovery after photobleaching (FRAP) experiment, we deposited SLBs on graphene surface which was transferred by PMMA and annealed in Ar / H_2 (50 % / 50 %) at 400 °C for 1 hour. Figure 3.3.(a) shows fluorescence image of SLBs on graphene surface before bleached. Then the fluorescent dye at the center of red circle with radius 30 μm is bleached in figure 3.3.(b). After 18.5 minutes, the fluorescence intensity at the center of red circle is recovered as the half of initial intensity in figure 3.3.(c). Figure 3.3.(d) presents that fluorescence intensity at the center of red circle recovers over time. The diffusion coefficient is 0.18 $\mu m^2/s$. The calculation is using following equation $D = 0.224 \times \omega^2/t_{1/2}$. D is the diffusion coefficient, ω is the radius of the photobleached spot and $t_{1/2}$ is the time at which half of the intensity was recovered[51].

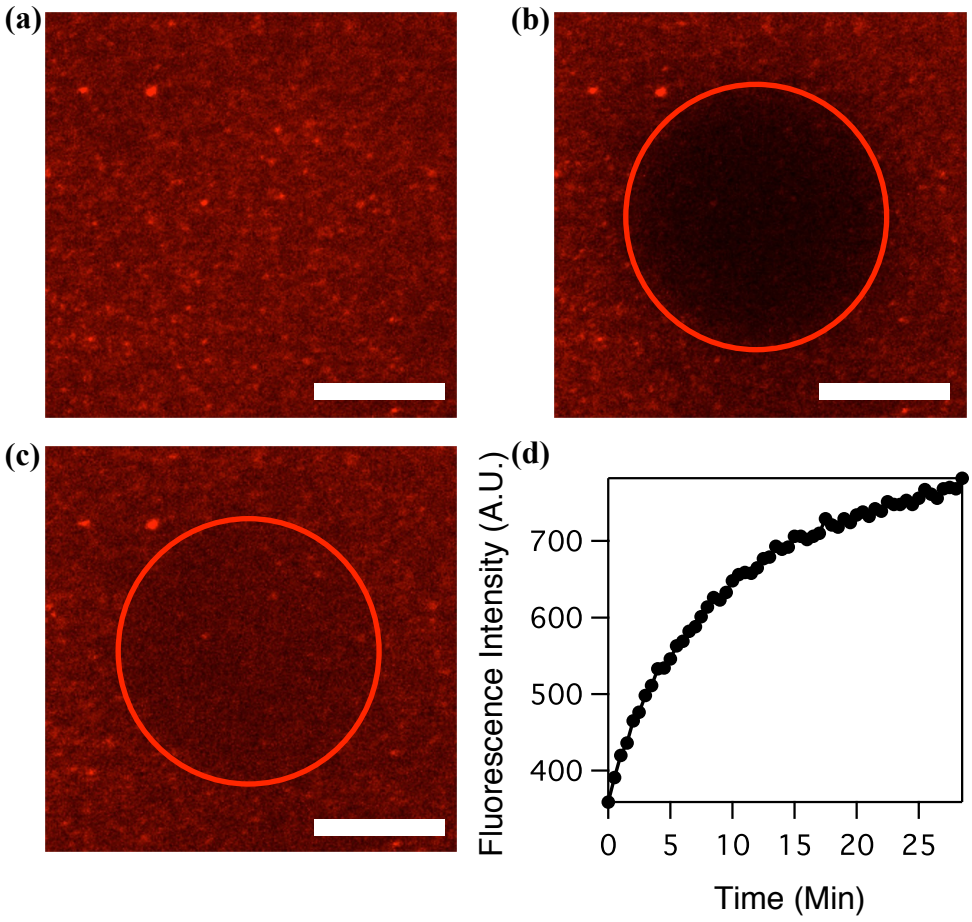

Figure 3.3. Fluorescence images of SLBs on graphene surface. (a) Before bleached. (b) After bleached at time 0. (c) After bleached at time 18.5 minutes. (d) Fluorescence intensity at the center of the red circle recovers over time. The scale bar is 30 μm.

3.3.4. ATOMIC FORCE MICROSCOPE IMAGES OF GRAPHENE AND SLBS

Figure 3.4.(a) is AFM image of SLBs on graphene surface. The deposition of SLBs is the same as written in the method of main paper. This image is scanned by contact-mode AFM in water. The SLBs presents uniformly and completely covering graphene surface. The z-axis scale

bar is from 0 to 16 nm. Figure 3.4.(b) presents the SLBs' height histogram of scanned area figure 3.4.(a). The height difference from the lowest point to highest point is less than 5 nm. The result shows that the surface of SLBs is very smooth and uniform.

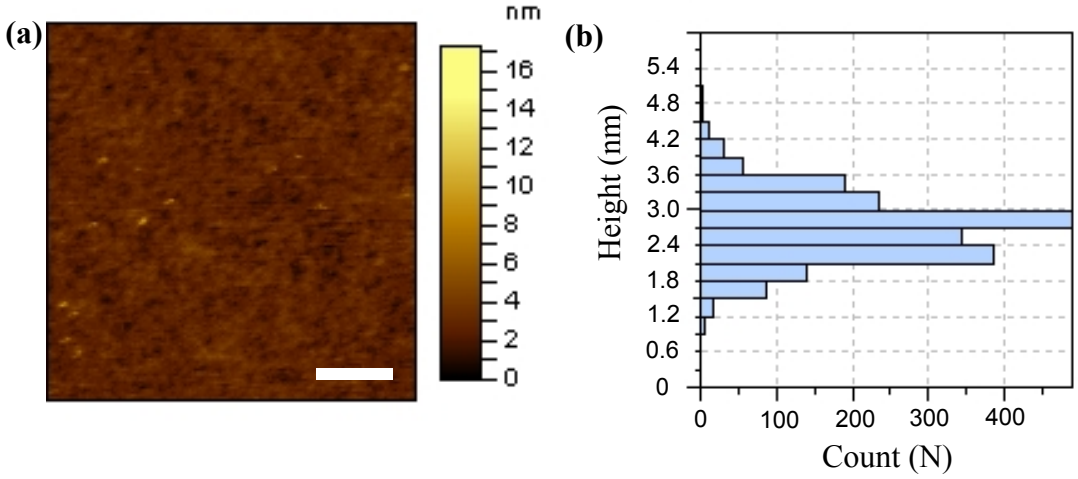

Figure 3.4. Atomic force microscope images. (a) SLBs on graphene surface taken by contact-mode AFM in water. The scale bar is 1 μm. (b) The SLBs' height histogram of scanned area figure (a).

3.3.5. CONTACT ANGLE MEASUREMENT OF GRAPHENE SURFACE

For the CVD-grown graphene on copper foil, the contact angle of water drop on graphene/PDMS is about 100˚(Figure 3.5.(a)). After the copper foil is etched, the contact angle is still about 100˚(Figure 3.5.(b)). Then the graphene is soaked in DI water for overnight as the standard procedure for depositing SLBs. The graphene surface is maintained in wet condition when dropping the water. Then contact angle of drop water on graphene surface changes from

100˚ to 45˚ (Figure 3.5.(c)). This indicated the transformation of graphene surface from hydrophobic to hydrophilic. This is due to the adsorption of hydrophilic OH groups on graphene surface after graphene is soaked in DI water for overnight. Because of hydrophilic surface, it is more favorable to form the supported lipid bilayer on graphene. Then the same sample is dried for overnight. The contact angle is back to 100˚(Figure 3.5.(d)). The graphene surface becomes hydrophobic after graphene surface is totally dry.

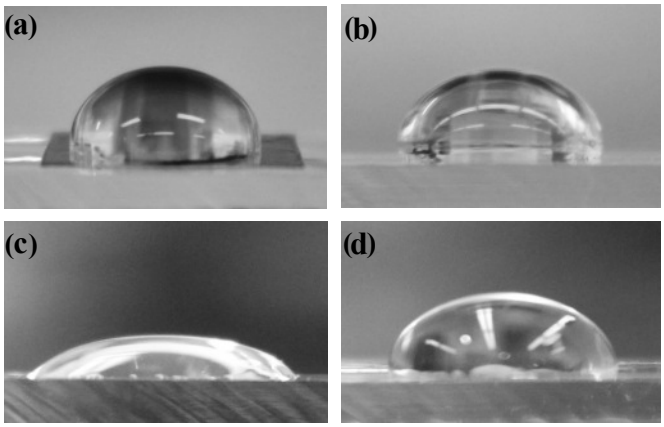

Figure 3.5. (a) CVD-grown graphene on copper foil. (b) Graphene is transferred on PDMS. (c) Graphene is soaked in DI water for overnight. (d) Graphene is dried for overnight.

3.3.6. THE CIRCUIT DIAGRAM

Figure 3.6.(b) presents a simplified equivalent circuit model. (A more detailed circuit model is presented in the figure 3.7.). We are mostly interested in the pulse shape and height, i.e. transients in response to opening and closing of ion channels. Therefore, the capacitances are of primary interest here. We model the system as two capacitors in series: The first is the well-

known lipid bilayer membrane capacitance $C_{membrane}$ (from prior studies as well as our own measurements described in the supporting information 3 to be ~ 0.6 μF/cm^2). The second capacitance is the graphene capacitance, which consists of two components in series: The electrochemical double layer capacitance and the quantum capacitance are in series, together forming C_g. We now discuss the quantum capacitance and the double layer capacitance in more detail.

The physical origin of the quantum capacitance is due to the following effect[52]: Adding electrons to a quantum system (e.g. a gas of many electrons, such as the electrons in a sheet of graphene) increases the Fermi energy of that system. Due to the Pauli exclusion principle, the lowest occupied quantum states are already filled and only the next available quantum states in the system can be filled with the addition of additional electrons. Adding N electrons increases the Fermi energy by the density of states times the number of electrons added, and one can equate this increase in energy with a capacitance (called the *quantum capacitance*), given by $\Delta E = Q^2/2C_{quantum}$. In general, unless the dimensions of the system are small, the spacing between each energy level in the system is very small compared to kT, and therefore the discreteness of the energy levels (i.e. the quantization of the energy levels) is not observed. (In other experiments where all 3 dimensions are small, the discrete quantum states can be observed, and these are called quantum dots. Our system is much too large in size to see quantum dot effects.) Therefore, the term quantum capacitance does not indicate a capacitance that is quantized. Rather, the quantum capacitance is a finite density of states effect. Normally in metals, the density of states is extremely large (due to the large electron density and Fermi energy), so that the quantum capacitance is also much larger than any other capacitance in the system, and hence does not appear in electrical measurements. In 2d and 1d systems with large geometric

capacitances (due to ultra thin and high K dielectrics *or* intimate physical contact with a gating electrolyte as in our system), the quantum capacitance is a significant component of the total capacitance of the system. How large is the quantum capacitance compared to the double layer capacitance in an electrolyte gated system? We now address that question for our particular system.

We first discuss the numerical value of the double layer capacitance C_{DL}. This consists of two physical capacitors in series: The Helmholtz capacitance $C_{Helmholtz}$, due to ions adsorbed directly on the surface, and the diffuse layer capacitance $C_{diffuse}$, due to a higher local ionic concentration of one charge species within a Debye length of the interface. The Helmholtz capacitance is typically independent of applied bias and around 10-20 $\mu F/cm^2$. Numerically, the diffuse capacitance can be estimated (at zero applied bias) as (ref.[53], eq. 13.3.21b) $C_{diffuse}=228\ C^{1/2}\ \mu F/cm^2$, where C is the electrolyte concentration in mol/L. At 0.1 M and 1 M, the prediction is $C_{diffuse}$ = 72 and 228 $\mu F/cm^2$, respectively. $C_{diffuse}$ has a mild bias dependence. Since the Helmholtz capacitance is much smaller than the diffuse layer capacitance, it dominates at the electrolyte concentrations used in this experiment, and the total double layer capacitance should be around 10-20 $\mu F/cm^2$, dominated by the Helmholtz capacitance, and only weakly dependent on applied bias. (See e.g. figure 13.3.1 of ref.[53], which shows 16-20 $\mu F/cm^2$ for 0.1 to 1 M NaF in contact with Hg, with very weak dependence on electrolyte concentration.) Note that the value of 0.1 mM to 1 mM used in ref.[42] is in a different regime, where the diffuse layer is the dominant capacitance and hence the total interfacial capacitance is strongly dependent on the electrolyte concentration. (See again e.g. figure 13.3.1 of ref.[53], which shows a strong dependence of the differential capacitance for NaF concentrations between 1 and 10 mM.) We next discuss the value of the quantum capacitance. Prior measurements of the quantum capacitance[42] put this

value at between 2 and 4 μF/cm^2 at the Dirac point, for impurity induced densities between 0.5 and 2 × 10^{12} cm^{-2}. Note that varying the electrolyte concentration can change the screening of impurities and hence the quantum capacitance. By this analysis, the literature seems to indicate that the quantum capacitance is significantly smaller than the double layer capacitance (2-4 *vs.* 10-20 μF/cm^2 at the electrolyte concentrations used in our experiments). This was not the case in ref.[42], where at low electrolyte concentrations the double layer capacitance would be predicted to be dominated by the diffuse capacitance, and be numerically comparable to the quantum capacitance.

Instead of relying on the literature, we have measured the total capacitance of graphene with no SLB using EIS (Figure 3.8.). We find a total value (including the quantum capacitance in series with the double layer capacitance) of between 2 and 5 μF/cm^2 at the Dirac point at the electrolyte concentrations used in these experiments. In the supporting information, we discuss in further detail the dependence of this measured capacitance on electrolyte concentration and composition, and compare to the only other measurement in the literature[42]. Although the detailed dependence on electrolyte concentration is not explained by existing theories, taken together our reasoning and data seem consistent with the consideration that the quantum capacitance is the dominant (smallest) capacitance compared to the double layer capacitance (specifically, $C_{quantum}$ ~ 2-5 μF/cm^2 and C_{DL} ~ 10-20 μF/cm^2), although current experimental techniques do not allow a separate measurement of each. Furthermore, as discussed further in the supporting information, the measured quantum capacitance *vs*. gate voltage for graphene with no SLB behaves as expected by the theory presented in ref.[42] for an impurity concentration of ~ 10^{12} cm^{-2}, a reasonable value consistent with the literature of graphene properties. Regardless of the relative contribution of each component, the measured capacitance is larger than the membrane

capacitance (measured separately, see supporting information 2), and this allows us to develop the simple circuit model in figure 3.6.(b) to analyze the electrical properties of our system.

The model in figure 3.6.(b) is intended to give a qualitative description of the pulse heights that confirms our interpretation of measurements of the opening and closing of ion channels. Because the graphene capacitance is larger than SLB capacitance, the system forms a voltage divider and most of the applied voltage drop is across SLB. In the case where there is a dc conductance across the bilayer, and from the solution to the graphene, the ratio of the conductances sets the dc voltages. As discussed in the supporting information, this does not qualitatively change the dc bias in our case. Thus, a 100 mV bias from graphene to counter electrode provides a ~90 mV voltage across the lipid bilayer membrane.

We next discuss what happens when the channel opens. When the ion channel opens, the resistance in the model R_{gA} changes from an open circuit to 100 GΩ. As the initial voltage is 90 mV, an initial current of ~ 0.9 pA flows through the ion channel (the resistor R_{gA} in the model). As this initial current flow, it charges the two capacitors. A simple model shows that in the limit where $C_g >> C_m$ (which is approximately true in this case), the current through the entire loop (which is measured by the current amplifier in our setup) is approximately equal to the current flowing through the ion channel. The exact expression is: $I_{measured} = (C_g/(C_g + C_m))\ I_{gA}$, where I_{gA} is the current flowing through gA ion channel. Thus, when the ion channel opens, most of the current is used to directly charge the quantum and interfacial capacitance of the graphene.

How long does the current flow and how does the amplitude change with time during the open period of the ion channel? As the charges on the capacitors change, so does the voltage across the lipid bilayer and the current flowing through the ion channel I_{gA}. However, the change

in voltage is very small for times of order 1 second or less, which is the timescale that the ion channel is open in our experiments. As the initial current flowing through the ion channel is approximately 90 mV/R_{gA} ~ 1 pA, this would change the voltage by the capacitors at a rate of 10^{-3} V/s or less. Within the one second time constant of the channel open or close time, this corresponds to a negligible change in the lipid bilayer voltage, and hence a negligible change in the current through the channel. Thus, the current *vs*. time is expected to be a step function, as is observed in our experiments. Note that we do not see any evidence of local changes in the ionic concentration in the water layer between the graphene and SLBs. Such a change might, for example, through various mechanisms cause a drop in the current while the ion channel was open; in contrast we observe a constant current during the open period. A more detailed model which includes the resistances of the membrane, the electrolyte resistance, and also any faradaic current between the graphene and the solution, does not alter this conclusion (Supporting information 1). Note that this is in sharp contrast to our comparable nanotube ion channel experiments[43-45], which has shown spikes in the current under identical experimental conditions, due to the small intrinsic capacitance of the nanotubes in a similar setup.

There are two physical effects that we next consider. The first is the dependence of the capacitance on the concentration of ions and voltages in the circuit, which both depend on time. The second is the possibility of non-uniform charging of the capacitances, which are distributed spatially. We discuss these both in turn.

Firstly, the circuit model in figure 3.6.(b) assumes the capacitances are all independent of time. However, in principle this is not true. For the simple case of an electrolyte in contact with a metal electrode, it is by now well established that the double layer capacitance depends on the dc

potential applied between the electrolyte and the metal electrode[53]. Therefore, if this dc potential changes with time, the capacitance will also change with time. In addition, the quantum capacitance of graphene depends on both the electron Fermi energy, i.e. electron density (which is also related to the applied dc potential, which will change in time as the various capacitors in the circuit are charged up), and the impurity density (which may change with time if the local ion concentration of the water layer between the graphene and the SLB changes). Prior to opening of the ion channel, our estimates above indicate that 90% of the voltage applied between the counter electrode (i.e. Ag/AgCl electrode in the electrolyte) and the graphene is dropped across the lipid bilayer membrane. Therefore, for an applied voltage of 100 mV, only 10 mV is applied between the water in contact with the graphene and the graphene itself. When the ion channel opens, this changes the applied voltage by an amount of roughly 10^{-3} V/s across the membrane, and 10^{-4} V/s between the water and the graphene. This would mean a change of less than 0.1 % of the quantum capacitance during the 1 second time the ion channel is open, and an even smaller change in the double layer capacitance during the same time (Figure 3.8.). Because the ionic strength of the electrolyte in contact with the graphene can change the graphene to electrolyte capacitance (Figure 3.8.), it is also possible that this changes with time. Although we do not know the exact ion concentration *vs*. time for the aqueous layer between the graphene and the bilayer, we can estimate that it is roughly comparable to the concentration of the bulk electrolyte. Using our data in figure 3.8. to estimate the change in capacitance with changes in the electrolyte concentration, we estimate that the percentage change in the graphene quantum capacitance due to the change in ionic strength is negligible during the measurement time. Thus, none of the physical effects that cause time dependence of the capacitances in our system is significant enough to change the measured ion channel current within the resolution of our

system. Finally, the in plane conductance of graphene will change with time due to the changes in the ionic concentration and voltages with time. However, since the graphene is highly conductive in plane compared to the impedance of the capacitors and the resistance of the bilayer and ion channel, the change in the in plane conductance will have a negligible effect on the ion channel current.

An important question is the effect of local ionic buildup. Our circuit model assumes the charge spreads quickly over the entire area. However, this is likely not the case, as there is bound to be significant spreading resistance in the lateral direction in the region between the SLB and the graphene electrode[54]. In our case, this would result in a smaller effective area that is charged. Thus, the ion channel current may not be charging the entire ~ mm^2 area in ~100 ms. However, as long as the spreading resistance is less than the individual ion channel resistance when it is open (approximately 100 GΩ for gA), this will not significantly change the shape of the current pulse.

Because at present we do not have a reliable way to measure the ion concentration in the water layer between the SLB and the graphene, we do not know the exact value of this quantity. In fact the exact thickness of the water layer is not certain in our measurements. However, it is clear from the electrical data that the magnitude and the time of the current spikes is consistent with a water layer that is thick enough to sustain an ionic current through the ion channel protein for the period of time that it is open, i.e. 10s of milliseconds. In the future, additional experimental techniques such as x-ray or neutron scattering will be required to quantify the exact distance between the SLB and the graphene in our system, a project which is currently underway in our labs.

Although a simple model of a uniform lipid bilayer is consistent with the time constant and magnitude of the current spikes, the frequency of current spikes is much less than would be expected given prior literature on gA incorporation into large area SLBs and the resultant change in the net resistance of the bilayer (i.e the time average)[55]. This could be due to one of several factors. First, the incorporation efficiency of the ion channels could be very low in this system. Second, it is possible that there are patches of multilayer and bilayers simultaneously present; when an ion channel is incorporated into a bilayer, current spikes are registered, but when an ion channel is incorporated into a multilayer, no current spikes are registered. This is consistent with the EIS measurements which indicate, in some cases, the presence of predominantly multilayers, as measured by the capacitance of the membrane in our circuit model (Figure 3.6.(b)). Finally, although we consider this unlikely, it is possible that the channels are denatured somehow by the graphene itself. We note that none of these interpretations would change the conclusion that each individual ion channel is charging predominantly the quantum and interfacial capacitance of the graphene, as it is still the dominant capacitance in the circuit.

We now compare these results to those obtained in the literature on comparable systems using metal electrodes in place of the graphene used in our experiments. The group of Duran has measured single ion channel currents through gA using lipid bilayers covalently tethered to Au[56]. There, they observed approximately the correct current but the lifetime was 100x smaller than our measured lifetime of gA and that of suspended bilayer measurements of gA, with no explanation given. Follow on measurements by the same group gave a measurement of *M2δ*[57], *BK*[57], *MscL*[58] with 3-10x lower conductance, but comparable lifetimes to those same ion channel proteins in suspended lipid bilayers. Guidelli has measured single ion channel alamethicin on metal electrodes and compared two different methods to form the bilayers: drop spilling, and

vesicle fusion[59,60]. He found a lower conductance but comparable lifetime to suspended bilayers using vesicle fusion method, but a conductance as in suspended but a smaller lifetime with drop spilling, indicating that the lipid preparation has a significant impact on the measured electrical properties, and possibly unfused vesicles forming local liposomes with incorporated ion channels complicating the measurement and blocking the measured current so that the conductance measured is not that of a suspended membrane ion channel. In our measurements, as we do not have a covalent tether, we speculate that this allows our ion channels to more freely diffuse in the plane, and allows us to more closely measure both the lifetime and conductance level that is comparable to the values of these ion channels in suspended membranes, in contrast to the metal electrode measurements published to date. However, this issue deserves further research, as the lipid bilayer deposition chemistry can most likely be tuned and optimized much further than our initial proof of concept demonstration of single ion channel sensing with graphene.

In the experiments presented here, the graphene acts as an electrode, whose conductance is large compared to the individual ion channel. Therefore, the change in the in plane conductance of the graphene layer due to the ionic currents flowing through the membrane protein is not registered in our setup; the graphene acts as an atomically thin electrode. In addition, as we are limited in bias range to protect the fragile lipid bilayer (typically to p/m 100 mV), the Dirac point of the graphene does not always fall within the bias range of the ion channel experiments. However, local capacitive charging of the graphene at the nanoscale may change its plane transport characteristics, an exciting area to extend our work to future sensing modalities. In the future, it would be interesting to extend these measurements to include the measurements of the source-drain current in response to the ion channel currents.

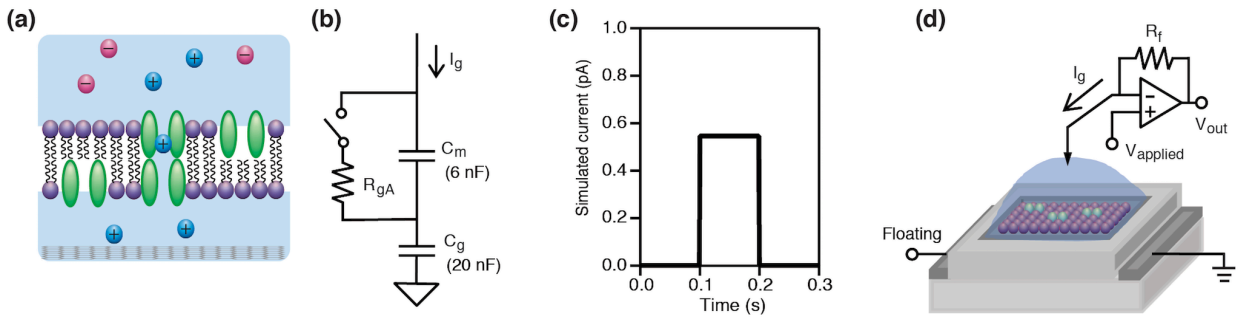

Figure 3.6. (a) Schematic diagram of SLBs with gA on graphene surface. (b) Circuit diagram of graphene-SLBs. R_{gA} represents a single ion channel gA that is either open (R_{gA} ~ 100 GΩ) or closed (R_{gA} an open). $C_{membrane}$ is the capacitance of SLBs, measured to be 0.6 μF/cm^2 and scaled to the 1 mm^2 area of our system. $C_{quantum}$ is the capacitance of graphene, measured to be 2 μF/cm^2 and scaled to the 1 mm^2 area of our system. (c) Simulation result of current detected by patch clamp system. (d) Schematic diagram of SLBs on graphene FETs connected with patch clamp system.

3.3.7. THE EXPANDED CIRCUIT DIAGRAM

The simplified circuit diagram (Figure 3.6.(b)) contains all the essential components, but here we discuss the additional components, determine their values, and discuss why they do not significantly change the conclusions of the manuscript. Figure3.7. shows a more complete equivalent circuit for our device which we now discuss.

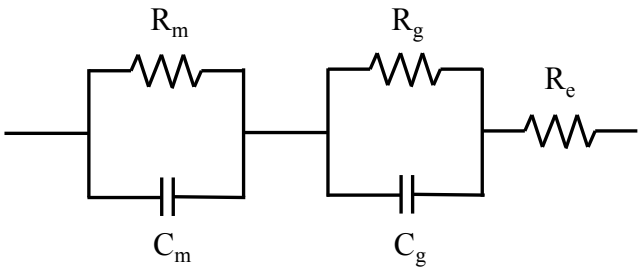

$$Z = R_e + \frac{R_m(1 + j\omega R_g C_g) + R_s(1 + j\omega R_m C_m)}{(1 + j\omega R_g C_g)(1 + j\omega R_m C_m)}$$

Figure 3.7. Equivalent circuit model with two time constants**.** R_e is the electrolyte resistance, R_g is the charge transfer resistance of the graphene/electrolyte interface, C_g stands for the double layer capacitance of the graphene/electrolyte interface in series with the quantum capacitance of the graphene sheet. R_m and C_m are the lipid layer resistance and capacitance.

The electrolyte-graphene Faradaic current is expected to be small since we do not have a redox active species, and the applied potentials are within the window of voltage where the water is not electrochemically active. Based on the measured DC current from graphene to solution in the absence of SLBs, we estimate the value of R_g in the circuit to be ~ 10 MΩ. After addition of the lipid bilayer, this rises to ~ 500 MΩ. Thus we estimate the bilayer membrane resistance R_m to be ~ 0.5 GΩ. Both of these resistances were determined by dc measurements (see main text), but also verified by electrochemical impedance spectroscopy, discussed below. From a circuit point of view this resistance is large enough that it does not perturb the currents significantly. The electrolyte, reference electrode and contact resistances all shown by the series resistance (R_e = 20 kΩ), small enough that it does not significantly perturb the currents flowing through the gA channel (R_{gA} = 100 GΩ).

The circuit diagram is simulated in a circuit simulator. It is assumed the gramicidin channel has a resistance of 100 GΩ and remains open for 0.1 seconds. The simulation result of the current step is measured by the patch clamp amplifier (Figure 3.8.(b)). The result is similar to our ion channel measurements (Figure 3.6.(f) and 3.6.(i)) and shows the leakage resistors do not affect the behavior of the system significantly.

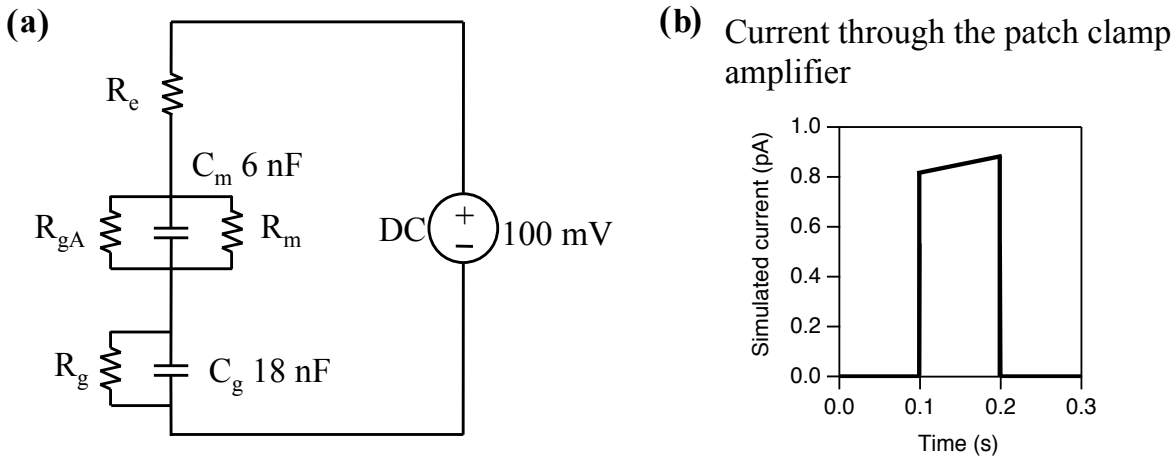

Figure 3.8. (a) Circuit diagram of graphene-SLBs. (b) Simulation result showing the current sensed through the patch clamp.

3.3.8. MEASUREMENT OF QUANTUM AND INTERFACIAL CAPACITANCE

To measure the capacitance between the electrolyte and the graphene, we measured the electrochemical impedance spectrum (EIS). Two setups were used both giving consistent results: a custom built electrochemical impedance spectrometer based on a lock-in amplifier and a signal generator, and a Gamry automated system (model Reference 600). The impedance of the device is measured over the frequency range of $10^{-2} \sim 10^{4}$ Hz, with 7 points per decade.

Figure 3.9. presents a typical electrochemical impedance measurement of bare graphene in 100 mM KCl. The black line is measured data and red line is fitted data. The bare graphene capacitance is 2 μF/cm^2 that was measured in 100 mM KCl.

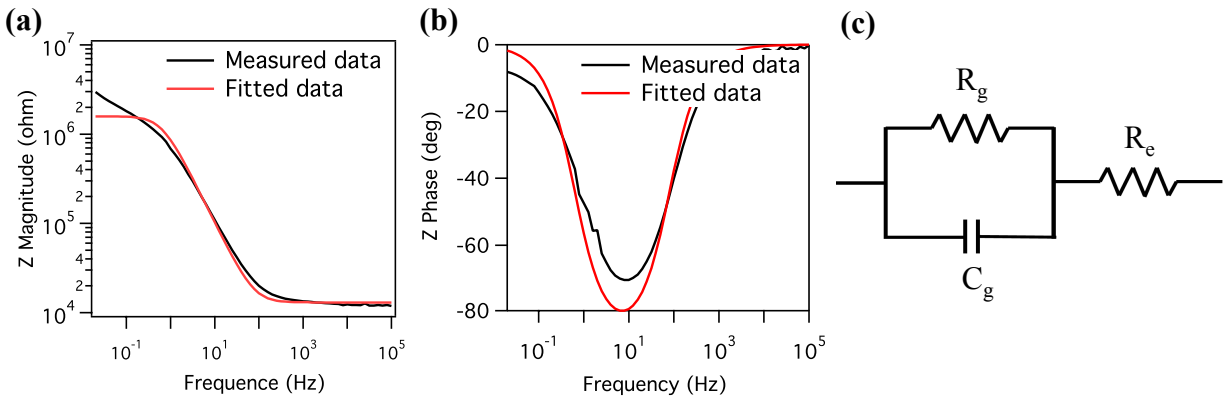

Figure 3.9. Electrochemical impedance measurement of bare graphene.

We performed this experiment using two different concentrations on over 20 separate devices, and present a histogram in figure 3.10. for the total capacitance. In the case of 1 M CsCl, the average total capacitance is 2 μF/cm^2. In the case of 100 mM KCl, the average total capacitance is 5 μF/cm^2. Also shown are the only other measurements in the literature[61], at 0.1 and 1 mM NaF. All of the values are comparable, but there is considerable spread. It is likely that device to device differences are due to different impurity concentrations in different devices, which are known to effect the quantum capacitance[61]. At present there is no theoretical explanation for the dependence of the value on the electrolyte concentration or composition, a question that is currently under investigation.

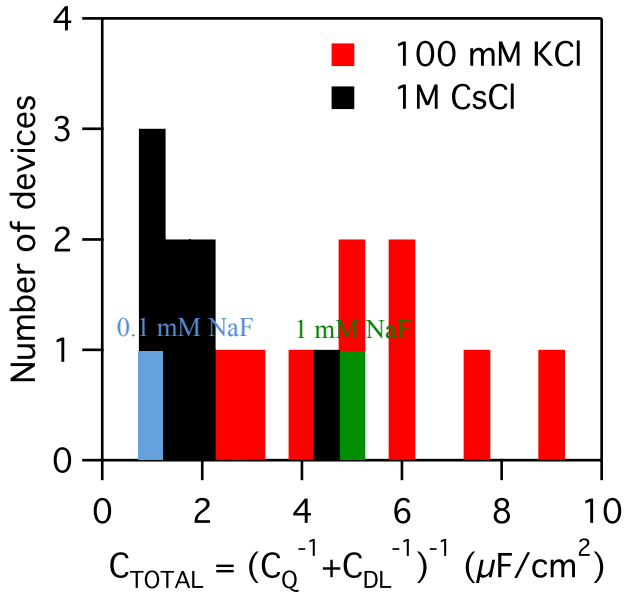

Figure 3.10. The number of experiment versus total capacitance.

In order to determine experimentally the effect that different concentrations would have on the capacitance, we measured the voltage dependent capacitance in different concentrations using the same device. The results are presented in figure 2.11. The voltage dependence is consistent with an impurity concentration of ~ 10^{12} cm^{-2}, according to ref. [61].

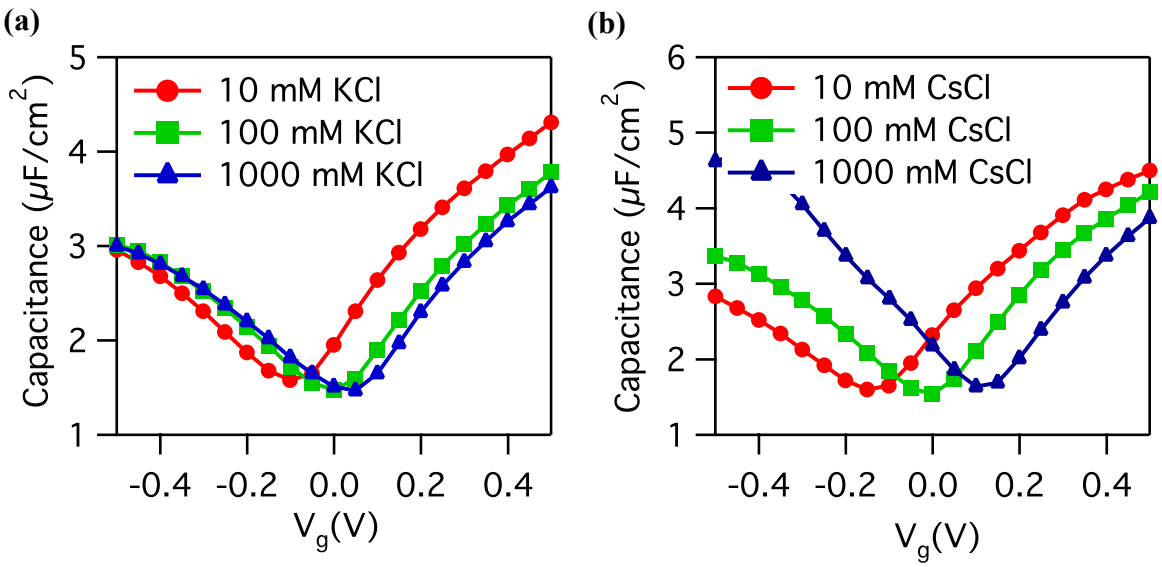

Figure 3.11. The capacitance as function of gate voltage in different concentration of (a) KCl and (b) CsCl.

3.3.9. MEASUREMENT OF LIPID BILAYER CAPACITANCE

To measure the lipid bilayer capacitance we next added the SLB and measured the EIS. The two time constant circuit model shown in figure 3.6. is used to fit experimental data. The EIS is shown in figure 3.12.

Circuit parameters are estimated by curve fitting to the Bode plot (Figure 3.12.). About 30% of devices have a lipid capacitance of 0.6-0.7 μF/cm^2, which is characteristic of a lipid bilayer. For other devices the capacitance is either around 1-1.3 μF/cm^2, showing the formation of a lipid monolayer on graphene, or around 0.2 μF/cm^2, indicating presence of multiple lipid layers on graphene.

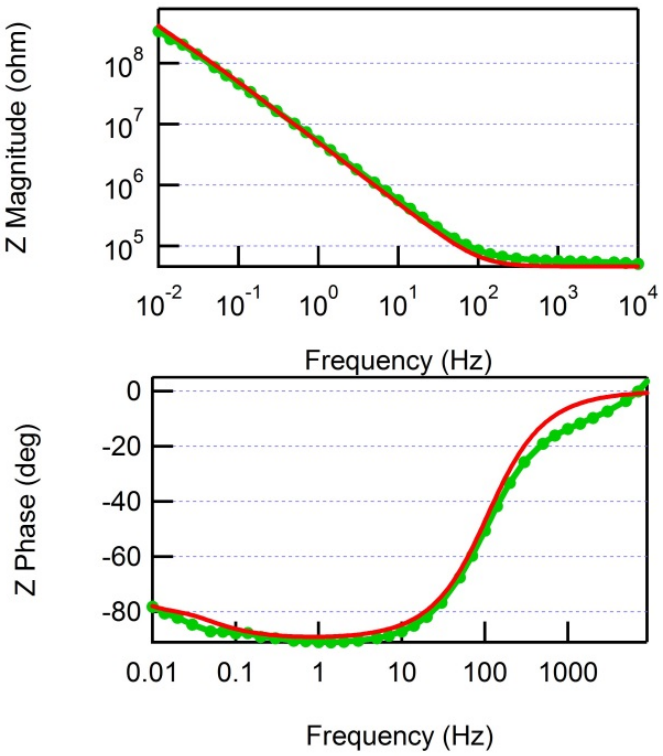

Figure 3.12. Measured bode plot of the device capacitance (green curve) and the curve fitted to the data (red curve).

3.4. DISCUSSION

3.4.1. GRAPHENE AND LIPID BILAYER PLATFORM

Prior to deposition of the lipid bilayer, the electrolyte (0.1 mM phosphate buffer at pH 7 with 100 mM KCl) allows liquid top gating of the graphene in plane conductance. The electrolyte does not contain a redox active species, and so within the voltage window applied by the

Ag/AgCl elecrtrode (which we refer to as the gate voltage V_g), we expect no faradaic current, i.e. we expect no electron transport from graphene to solution. Measurements of the graphene to electrolyte current (which we call the "gate current") confirm this: The current from the graphene to the electrolyte (the background current) is less than 15 nA in the range of applied gate voltage[49]. The physical origin of this current is likely trace redox active species, or background redox of OH^- and H^+, both of which are small as expected. (Prior work[62] shows an expected "background" current of less than 5×10^{-4} A/cm^2, which would translate into less than 100 nA in our geometry). This confirms that the electrolyte is only capacitively gating the graphene and not allowing a significant amount of direct dc current to flow from graphene to the electrolyte.

Once the basic device was operating without the bilayer, we turned to formation of a lipid bilayer on graphene. Formation of SLBs was performed by the vesicle fusion method. Briefly, lipids in chloroform solvent are evaporated under nitrogen. The dried lipids are solubilized in phosphate buffer solution to form a multilamellar vesicle (MLV) solution. Small unilamellar vesicles (SUVs) are obtained by sonication of the MLV solution. SLBs are deposited on graphene transistors by heating the SUV solution in contact with the graphene surface. This process involves adsorption, deformation, flattening and rupture of the vesicles on the graphene surface. The lipid bilayers are then rinsed abundantly with deionized water to form continuous SLBs. Formation of SLBs on graphene has also been reported by another group[63]. Typically, continuous and uniform supported lipid bilayers can only form on a surface that is hydrophilic, with a layer of water trapped between the hydrophilic lipid heads and the hydrophilic surface. Although this was not addressed in Ref.[63], the reason that both that group and our own are able to form continuous, high quality SLBs on graphene is most likely related to the fact that graphene is not entirely hydrophobic, and its surface properties are closely related to the supporting

substrate[64,65], which can even render it hydrophilic in some cases. A key issue for the end result in this experiment is the uniformity, quality, and seal of SLBs. Initially, a simple fluorescence image (using 1 mM of fluorescent dye solution (rhodamine DHPE) added to label lipids hours before evaporation of chloroform) indicates that the bilayer is smooth and continuous (Figure 3.1.(a)). FRAP and AFM data confirm this interpretation (Figure 3.3. and figure 3.4.). However, more comprehensive analysis of the seal was assayed in several ways, discussed in more detail next.

The dc transport data in the presence of the lipid bilayer indicates that the in plane graphene conductance is still gated by the electrolyte through the lipid bilayer, with a small shift of the Dirac point figure 3.13.(d). The interaction of the lipids with the graphene, while not the focus of this work, was studied extensively in Ref.[63], where the change of the Dirac voltage with lipids of different head charges was studied in detail. Although they did not report the quantitative difference between the Dirac point with pure water *vs*. lipids, and they did not study the pH or electrolyte concentration dependence of the Dirac point as we did (see below), our results are qualitatively consistent with Ref.[63]. For the detection of single ion channel activity, a low-leakage current between the graphene and the electrolyte is necessary, as one generally needs a stable and high electrical resistance of SLBs in the gigaohm range for high quality electrophysiology. In figure 3.13.(c), the effective resistance of the graphene-electrolyte interface is about 35 MΩ. After the graphene is covered by SLBs, the effective resistance between the graphene and the electrolyte increases by over an order of magnitude to about 0.5 GΩ, indicating a high quality, electrically insulating layer has been formed by the lipid bilayer. As our area is 1 mm^2, this results in a specific resistance of about 10 MΩ-cm^2, a very high specific resistance for

SLBs[37,66,67]. With this GΩ seal, our graphene-SLBs devices are primed to detect single ion channel activity.

The presence of a uniform fluorescence image and high resistance seal does not confirm whether the system is a lipid monolayer, bilayer, or multi-layer. Even FRAP is unable to convincingly determine if there is a bilayer or multilayer. Therefore, the one prior claim in the literature of a single bilayer on graphene[63] cannot rule out the possibility that a multilayer was present. Therefore, to date no convincing evidence of a single bilayer on graphene has ever been presented. In order to assay the number of bilayers in our samples, we have used electrochemical impedance spectroscopy (EIS, see figure 3.9.) to determine the capacitance of SLBs. This is the "gold standard" in electrophysiology to determine the properties of the lipid bilayer, with an expected value of around 0.7 $\mu F/cm^2$. In our experiments, around 30% of devices have a lipid capacitance of 0.6-0.7 $\mu F/cm^2$, which is characteristic of a lipid bilayer. For other devices the capacitance is either around 1-1.3 $\mu F/cm^2$, showing the formation of a lipid monolayer on graphene, or around 0.2 $\mu F/cm^2$, indicating presence of multiple lipid layers on graphene. In order to confirm this interpretation, we performed another test based on fluorescence quenching (Figure 3.2.). The working principle is that QSY-7 amine can quench, via FRET, the fluorescence of the lipid dye reporter TexasRed DHPE (Invitrogen #T1395MP) embedded into the lipid layer. If a supported lipid bilayer is truly a bilayer, only the top layer is accessible to QSY-7 amine and therefore adding the quencher will reduce roughly half of the total fluorescence intensity. Similarly, the reduction will be less if the lipid layer is a multilayer. Of all the devices we tested, 30% showed approximately 50% decrease in fluorescence intensity, indicating the formation of a true lipid bilayer. FRAP and AFM data confirm this interpretation (Figure 3.3. and figure 3.4.).

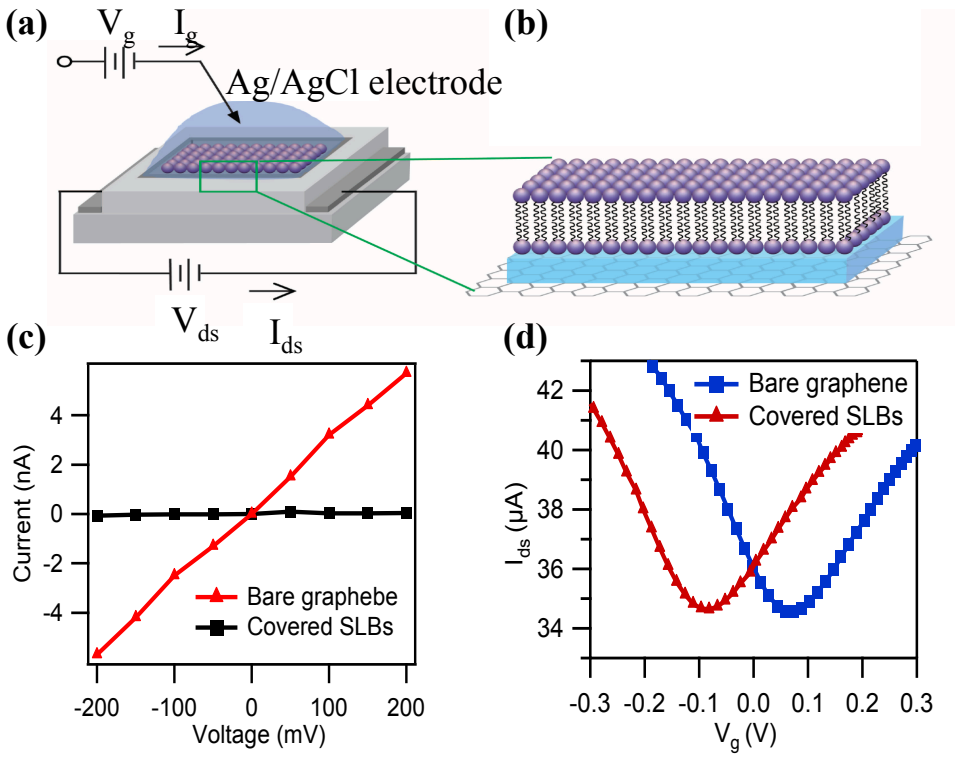

Figure 3.13. (a) Schematic illustration of graphene-SLBs platform. (b) High magnification illustration of SLBs on graphene surface. (c) The drain-source current *vs.* liquid gate voltage characteristics of bare graphene FET and covered by SLBs at 100 mM KCl and V_{ds}=100 mV. (d) The liquid gate current *vs.* liquid gate voltage characteristics of FET with bare graphene and covered by SLBs at 100 mM KCl.

3.4.2. THE EFFECTS OF GRAPHENE'S DIRAC POINT WITH LIPID BILAYER

In building a sensitive and selective biosensor platform, it is critical for the devices to maintain both graphene's extreme sensitivity and the SLBs' chemical and electrical isolation from the electrolyte environment. Once this is demonstrated, the SLBs can be functionalized to

specific analyses for selective biosensor applications. Therefore, we next demonstrate the bare graphene transistors' sensitivity and the SLBs' seal performance.

To understand in more detail the effects of SLBs on the graphene surface, we examined bare graphene FETs and those covered with SLBs as a function of electrolyte (KCl) concentration as well as pH. Figure 3.14.(a) shows depletion curves (drain-source current I_{ds} *vs*. electrolyte gate voltage V_g) of bare graphene transistors for three different KCl concentrations (10, 100 and 1000 mM), showing the typical V-shaped transfer curves. When the ionic strength is increased, the Dirac point is shifted negative (consistent with previous reports[68,69]). Figure 3.14.(b) demonstrates that this sensitivity of the Dirac point to KCl concentration is completely removed after deposition of SLBs, indicating that SLBs form an effective chemical and electrostatic barrier between the graphene and the electrolyte solution.

Next, we investigate the sensitivity of the Dirac point to solution pH. Figure 3.14.(c) presents depletion curves of bare graphene transistors for three different pH values (4, 7, and 10 pH), all showing the typical V-shaped depletion curves. The Dirac point has shifted positive with an increase in pH value from pH 4 to pH 10[70,71]. Similarly to the electrolyte case, we show that the Dirac point is completely unaffected by the electrolyte pH after deposition of SLBs (Figure 3.14.(d)). This provides further indication that the graphene is chemically isolated from the electrolyte after deposition of SLBs.

Taken collectively, by measuring the electrical current directly through SLBs, as well as the sensitivity of the Dirac point to changes in the electrolyte pH and concentration before and after deposition of SLBs, in addition to the bilayer capacitance and fluorescence, we provide strong evidence that the graphene is insulated from the electrolyte environment by SLBs. We next turn

our attention to the behavior of this system upon introduction of pore forming membrane proteins gA and alamethicin.

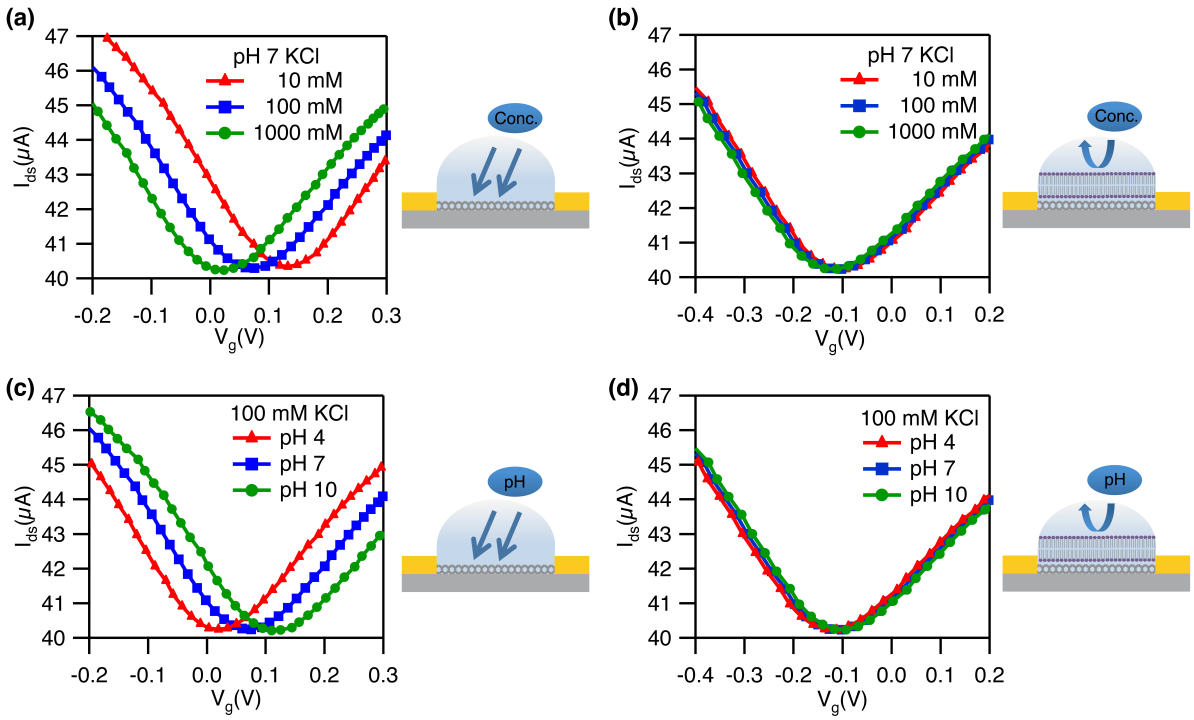

Figure 3.14. (a) Bare graphene FETs in 0.1 mM PB buffer at pH 7 with 10 mM KCl (red), 100 mM KCl (blue) and 1 M KCl (green). (b) Graphene FETs coating with SLBs in 0.1 mM PB buffer at pH 7 with 10 mM KCl (red), 100 mM KCl (blue) and 1 M KCl (green). (c) Bare graphene FETs in 0.1 mM PB buffer with 100 mM KCl at pH 4 (red), pH 7 (blue) and pH 10 (green). (d) Graphene FETs coating with SLBs in 0.1 mM PB buffer with 100 mM KCl at pH 4 (red), pH 7 (blue) and pH 10 (green). All measurement are conducted at V_{ds}=100 mV.

3.4.3. CURRENT TRACE OF ION CHANNEL GRAMICIDIN A AND ALAMETHICIN

Gramicidin A (gA) is a canonical (model) ion channel protein for demonstration of electrophysiology because of its simple behavior: It displays linear conductance with membrane voltage (i.e. it is a voltage independent channel), is permeable to monovalent cations, is stable at different chemical environments, and is easy to be modified to obtain various sensing applications[72,73]. Gramicidin A monomers (which diffuse laterally on both sides of the bilayer) occasionally dimerize (with a lifetime of order 1 second), forming a 4 Å wide and 25 Å long water channel for the conduction of monovalent cation current, with a conductance of order 10 pS (100 GΩ). In suspended lipid bilayer experiments, this results in a step function current *vs*. time trace with heights of order a few pA, and widths of order seconds. In order to investigate this for our lipid bilayer geometry, we introduce gA monomers into the SLBs prior to formation (Figure 3.15.(a)), and then measure the current through the SLB with a high resolution patch clamp amplifier system *vs*. time (see Methods).

Figure 3.15.(b) presents the current (between the graphene and the electrolyte, through the SLB) *vs*. time at 100 mV positive applied voltages between the electrolyte and the graphene. Clear, step function behavior is observed with the approximate expected amplitude (12 pA) and width (10s of ms) of the opening and closing of a single gA channel. From the histogram of the current trace (Figure 3.15.(c)), open and close events are apparent. At 50 mV positive applied voltage, the current step magnitude is 6 pA (Figure 3.16.), about half of the 100 mV step height, indicating a linear current voltage curve, as expected for gA. In order to further support our interpretation that the current steps are due to the opening and closing of individual ion channels, we decided to vary the type of membrane protein ion channel, while keeping all of the other procedures essentially identical. Our next ion channel to study is alamethicin.

Alamethicin is a voltage-gated channel-forming peptide[73]: when the membrane surface has sufficiently negative potential, the ion channel will form in the SLBs. Depending on the number of monomeric units forming the channel, different conductance levels are typically observed. The selectivity for ions is minimal but cations are somewhat preferred over anions (Figure 3.15.(d)). Thus, the key features of alamethicin (in particular, as compared to gA) are A) An asymmetric current-voltage relationship, B) multiple conductance values, and C) much larger conductance (~100 pS *vs*. ~10 pS) than gA.

Figure 3.15.(e) presents a representative time trace for the same experimental conditions as figure 3.15.(b) but with the only substantial difference that we use alamethicin instead of gA. A histogram of the currents clearly indicates multiple current values, typical of alamethicin which displays multiple conductance values (Figure 3.15.(f)). Alamethicin is known to have 5 conductance values in suspended lipid bilayers (which are not uniformly spaced), but of these the largest conductance state is rarely observed, and the smallest is very close to zero conductance compared to the other 4 states. This is completely consistent with our measurement, where we do not have enough signal to noise to resolve the first (lowest) conductance state and the highest conductance state is not observed in our measurement time. (A more detailed analysis in the figure 3.12. shows that the steps that we do observe are completely consistent with the multiple conductance states observed in the literature.) Similarly, the open dwell times are of order 100 ms, also characteristic of alamethicin. Finally, the current values (~ 100 pA) are about an order of magnitude larger for the alamethicin channels than the gA channels, as expected. These observations (higher current, multiple conductance states, and asymmetric current-voltage characteristics) are in agreement with well known properties of alamethicin ion channels[25]. The yields of observing ion channel activity are about 20% and 40% for alamethicin and gA,

respectively. Although we have not done a systematic study, this yield seems to improve with lower applied voltages across the lipid bilayer. At voltages larger than 0.5 V, this yield drops to zero. This is consistent with the known properties of both suspended and supported lipid bilayers.

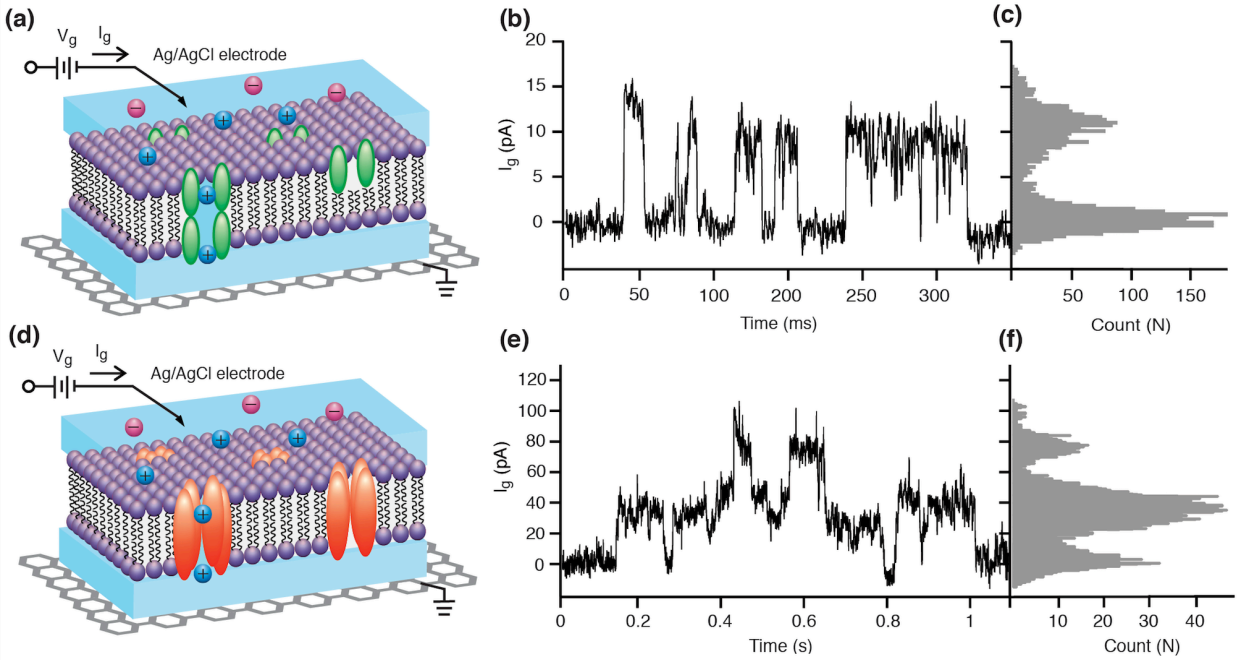

Figure 3.15. (a) Schematic diagram of SLBs with gA on graphene surface for ion channel activity detection. (b) Current trace for ion channel activity of gA at V_g=100 mV in 1 M CsCl. (c) Histogram of current trace a. (d) Schematic diagram of SLBs with alamethicin on graphene surface for ion channel activity detection. (e) Current trace for ion channel activity of alamethicin at V_g=100 mV in 100 mM KCl. (f) Histogram of current trace e.

3.4.4. CURRENT TRACES OF ION CHANNEL GA AT DIFFERENT BIAS

The SLBs with gA channels are deposited on graphene surface to detect single ion channel activity. The single ion channel activity is detected at the different applied potential from -100 to 100 mV (Figure 3.16.(a)). In the applied voltage 100 mV, the opening and closing events are observed. The current step is about 12 pA. In the 50 mV applied potential, the ion channel activity is also observed. The current step is about 6 pA. The gA is a voltage-independent ion channel. There is no effect of voltage on closing and opening ion channel. When gA ion channel is open, the Cs^+ ions can pass through from outside solution (1 M CsCl) of SLBs to inside solution water. Then the current steps are observed in the recording trace. We expect to see current steps of gA ion channel have systematic correlation with applied voltage. However, the negative current steps of gA are not observed at applied voltage -50 and -100 mV. Before the formation of SLBs, the graphene device is only soaked by distilled water overnight. Then lipid vesicles solution is added to form SLBs. The device is also rinsed by distilled water for several times. Therefore, there is only water existing on top of SLBs and between SLBs and graphene. When the ion channel measurement is conducted, the water will be replaced by 1 M CsCl solution. The SLBs is stable and continue to cover the graphene surface. The CsCl ions are not able to pass through SLBs. Therefore, only pure water exists between SLBs and graphene. When the negative voltage is applied, no CsCl ion can pass ion channel gA. Then no current steps can be observed in the negative applied voltage. The histogram of current trace at 100 mV is presented (Figure 3.16.(b)). The left peak is the baseline of current trace at 0 pA. The right peak is opened ion channel at 12 pA. Figure 3.16.(c) is the histogram of current trace at 50 mV. The baseline current is at 0 pA and the opened ion channel is at 6 pA.

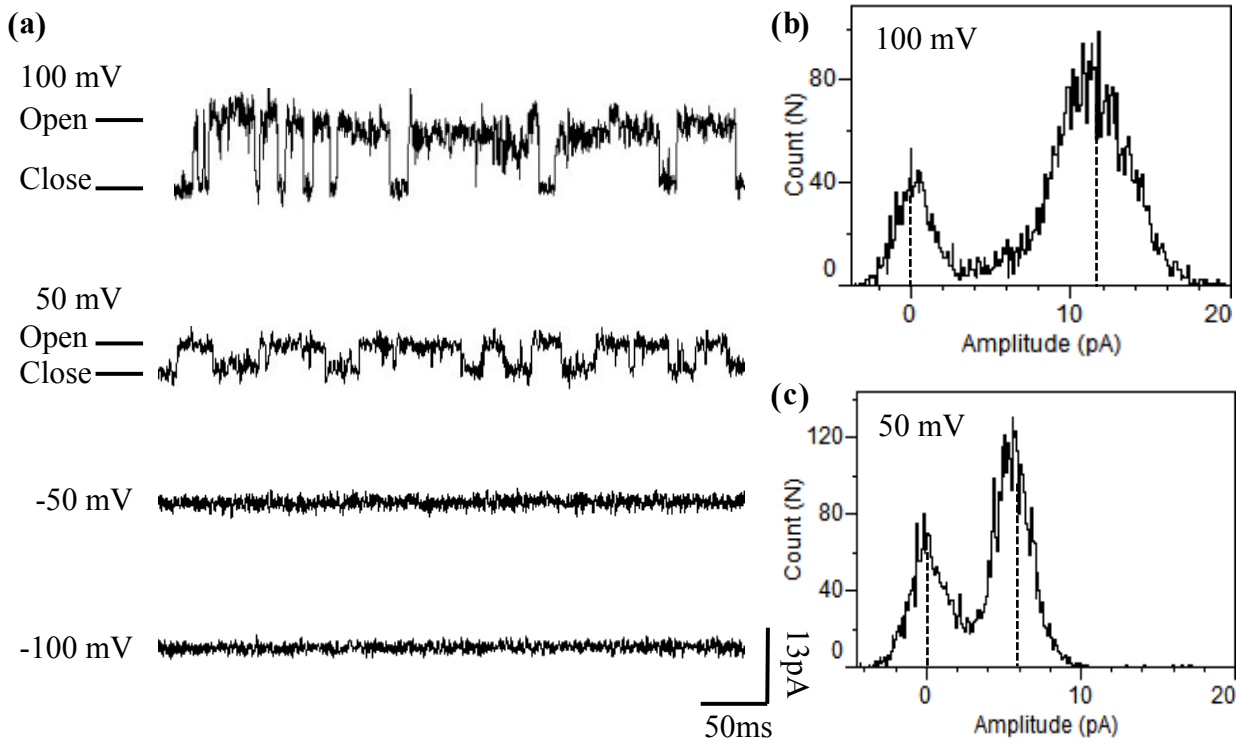

Figure 3.16. (a) Current traces are measured at different voltage from -100 mV to 100 mV. (b) The histogram of current trace at 100 mV. (c) The histogram of current trace at 50 mV.

3.4.5. CURRENT TRACES OF ION CHANNEL ALAMETHICIN AT DIFFERENT BIAS

Figure 3.17.(a) presents ion channel activity of alamethicin detected by graphene-SLBs devices at different applied potential from -200 to 200 mV at 0.1 M KCl solution. For 200 mV applied voltage, the current spikes of ion channel are about 120 pA. The open dwell times are from 50 to 100 ms. The second current trace is alamethicin channel activity in 100 mV applied

potential. The different levels of spikes are observed. The single current of each level is about 35 pA. The open well times are from 50 to 100 ms. There is no current spike observed during the recording when the applied voltage is in both -100 and -200 mV. Because the surface of SLBs has no negative charged, the alamethicin peptides are not able to form ion channels in the SLBs. The histogram of current trace at 200 mV is showed (Figure 3.17.(b)). The left peak is baseline of current trace at 0 pA. The right peak is current step at 120 pA while the ion channel is formed. Figure 3.17.(c) is the histogram of current trace at 100 mV. The multi-steps of current are detected.

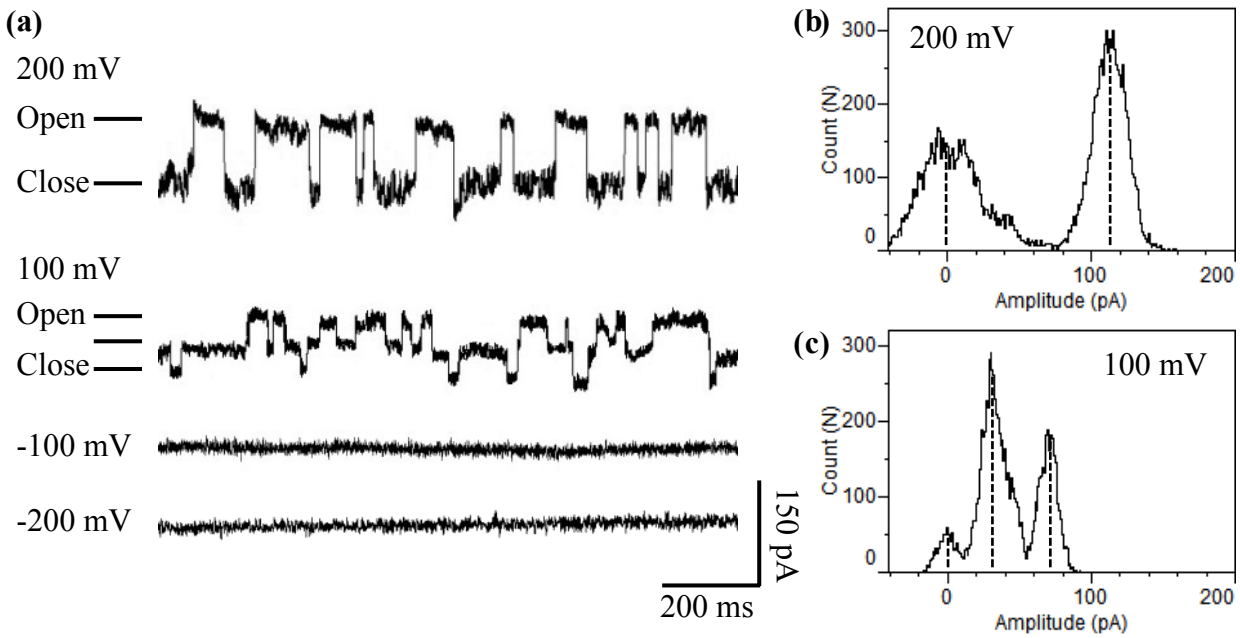

Figure 3.17. (a) Current traces measured at different voltage from -200 mV to 200 mV. (b) Histogram of current trace at 200 mV. (c) Histogram of current trace at 100 mV.

3.5. CONCLUSION

Taken collectively, this is strong evidence that we are indeed measuring the opening and closing of individual ion channels with graphene based electrodes. This represents a major milestone, as it demonstrates integration of nanoelectronics with electrophysiology, and opens many opportunities for integration of the two different disciplines. We anticipate that this general technique can be applied to any class of nanoelectronic device (top down or bottom up nanowires, nanotubes, other 2d materials, etc). A long-term dream of electrophysiologists has been to measure individual ions one by one as they pass through an ion channel. While this is not possible with traditional electrophysiology measurements, we speculate that approaches such as those demonstrated here, which combine advances in nanotechnology with qualitatively new measurements modalities of electrophysiology, may be the key to this holy grail of electrophysiology, opening new ways of unraveling ion channel currents with unprecedented levels of detail.

CHAPTER FOUR

POLYELECTROLYTE MULTILAYER ELECTROSTATIC GATING OF GRAPHENE FIELD-EFFECT TRANSISTORS

4.1. INTRODUCTION

Due to their planar nature and atomic thickness, graphene field-effect transistors (FETs) are potential candidates for a variety of chemical and biological sensors[74]. For liquid based sensors, most germane to physiologically relevant assays, a liquid electrolyte is typically in direct contact with the graphene surface. Broadly speaking the sensing assays can be divided into sensing three classes of moieties: (1) pH, (2) electrolyte concentration, (3) small quantities of charged analytes, especially charged biopolymers such as DNA[75] and proteins[76]. Because the liquid electrolyte or species to be sensed are in direct contact with the graphene, it is important to elucidate the physical interaction and mechanism of modulation of charge transport, especially the 3rd class (charged polymers).

In the case of the first two classes (pH and electrolyte concentration sensing), considerable controversy about the mechanism persists, in spite of general agreement that the mechanism is some combination of (1) changes of the surface charge density due to ionizable side groups or OH^- /H^+ adsorption, and (2) changes in the Debye layer screening of this surface charge. Dekker et al. presented a model of two ionizable impurities, both with pKa 4.5, one negative, and one positive that would be ionized at different pH[77]. They attributed this to residual resist and organics from the process of the fabrication, but argued that the graphene itself was pristine. Two other groups using different methods (electrochemical capacitance measurements[78], molecular modeling[79], as well as different substrate effects[80]), have argued against this hypothesis, claiming the OH^- and H^+ specifically adsorb to the sidewalls of pristine graphene, causing electrostatic gating effects. However, the molecular modeling was based on the assumption of graphene hydrophobicity, which is not always the case on hydrophilic substrates[81]. A third mechanism has

been proposed, in which ionization of dangling bonds at cracks or other graphene impurities changes in response to pH[82]. This is based on low pH sensitivity measured using putatively pristine (defect free) graphene, together with arguments of hydrophobicity being incompatible with OH^- or H^+ adsorption, which again neglects the hydrophilicity of graphene on hydrophilic substrates. In spite of this controversy, the mechanism of electrolyte and pH sensing is generally agreed upon to be due to two effects: Change of the surface charge and changes in the Debye layer screening of this surface charge.

In contrast to the first two cases, which have been well studied, the third and most important (and complex) case of the sensing of charged polymers has only been phenomenologically observed, but not studied in any model system. Given the potential technological significance of charged polymer sensing (in e.g. DNA sequencing, biomarker assays for cancer detection, etc.), it is important to elucidate the mechanism of sensing of charged polymers in graphene biosensors.

Nominally, graphene FETs detect the changes at the surface due to adsorption of charged species. These charged species may change the charge carrier density of graphene via one of two possible mechanisms. The first one is a capacitive gating mechanism like an electrostatic field effect transistor (gating). This mechanism does not involve the transfer of charge from the gating moiety to the graphene. For example, the applied voltage from the back of Si wafer or from the electrolyte solution to the graphene FETs will generate an electrostatic gating effect[77,83], even though no charge is transferred from the silicon back gate to the graphene. The second mechanism is surface charge doping by partial electron transfer to or from graphene. As an example of such charge transfer, a classical dopant in a semiconductor involves an atom which

"gives away" an entire extra outer shell electron to the conduction band of the semiconductor. Arguably, the most significant sensing applications of graphene will involve charged species (such as DNA and proteins, both charged biopolymers) which adsorb to the graphene surface. However, discerning the sensing mechanism (either doping or electrostatic gating) is non-trivial for charged species in direct physical contact with the surface of graphene, because both effects can contribute to the conductance change in response to adsorption.

In this work, we use a well defined charged polymer system (having both positive and negative charges determined at will) in direct contact with the graphene as a model system to investigate the interaction of charged polymer species with graphene. In order to study the exact nature of this interaction, we employed both positively and negatively charged multilayers polyallylamine hydrochloride (PAH) and sodium polystyrene sulfonate (PSS), respectively to mimic charged polymers on graphene's surface. These polyelectrolyte multilayers (PEMs) are prepared by the layer-by-layer deposition of polyanions and polycations from aqueous solution. With this technique, polyanion/polycation complexes are formed with charge reversal after each successive layer. Using these species, we can control and predict the shift of the graphene's Dirac point by the adsorption of different polymer layers, and effectively change the graphene from p-type to n-type at will. The Dirac point of graphene displays periodic behavior during sequential addition of positively and negatively charged polymers. A simple electrostatic model is applied to interpret these results, and demonstrates that electrostatic gating can account for the interaction of charged polymer species with graphene in an electrolyte gated system, the most promising sensing application envisioned for graphene biosensors. We compare this work to similar work on silicon on insulators, silicon oxide, silicon nanowires, and carbon nanotubes, each with a qualitatively different set of electrostatic and chemical properties, quite distinct from

graphene which presents a planar, nominally uniform, inert surface directly to the gating electrolyte.

4.2. METHODS

4.2.1. MATERIALS

Chemical Vapor deposition (CVD)-grown graphene was obtained from Graphene Supermarket. PAH (MW = 58,000) and PSS (MW = 70,000) were purchased from Sigma-Aldrich. The polyelectrolyte solution NaCl was prepared with deionized water obtained from a Millipore system.

4.2.2. FABRICATION AND MEASUREMENT OF GRAPHENE TRANSISTORS

The graphene transistors were fabricated by employing direct transfer CVD-grown graphene on a polydimethylsiloxane (PDMS) block[49]. Then a second PDMS well with a 2 mm × 5 mm window was attached on top of the graphene to insulate the solution from two electrodes. The electrolyte was 100 mM NaCl and the gate voltage was applied using a Ag/AgCl reference electrode. The drain–source current *vs*. gate voltage was measured using an Agilent 34401A multimeter.

4.2.3. DEPOSITION OF POLYELECTROLYTE PAH AND PSS ON GRAPHENE TRANSISTORS

The polyelectrolyte film was formed by dropping a solution of 1.5 mM PSS or PAH dissolved in deionized (DI) water in the PDMS open window on the graphene surface for 30 min. After the polymer solution was taken out, the graphene surface was rinsed with DI water several times. Finally, the polyelectrolyte film was dried at room temperature overnight. For the polyelectrolyte multilayers, the above process was repeated sequentially, alternating between PSS and PAH until the desired number of layers was achieved.

4.2.4. EQUIPMENT SET UP FOR CHARACTERIZATION

Scanning electron microscopy (SEM) images were obtained by FEI Quanta 3D FEG Dual Beam. Raman spectra were measured with a 532 nm excitation laser and a 50X objective lens. The specimens were prepared by PDMS transfer printing graphene onto SiO_2. Fourier transform infrared spectroscopy (FTIR) spectra were obtained with a PerkinElmer System 2000 FTIR. The samples for the FTIR were prepared by PDMS transfer printing graphene on calcium fluoride substrates.

4.3. CHARACTERIZATION

4.3.1. SEM IMAGES OF GRAPHENE, PAH/GRAPHENE AND PSS/GRAPHENE

The scanning electron microscopy is employed to investigate the deposition of PAH and PSS on graphene surface. Figure 4.1.(a) presents SEM image of the graphene surface. The graphene surface is clean without PAH and PSS. Figure 4.1.(b) is SEM image of graphene which is coated by PAH. Figure 4.1.(c) shows SEM image of graphene coated with PSS.

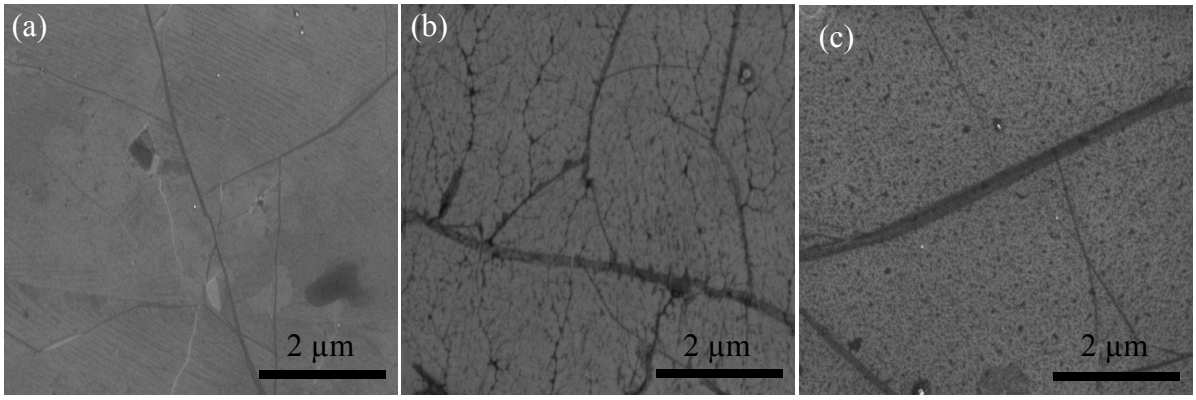

Figure 4.1. (a) SEM image of the graphene surface. (b) SEM image of graphene coated by PAH. (c) SEM image of graphene coated by PSS.

4.3.2. RAMAN SPECTRA OF GRAPHENE, PAH/GRAPHENE AND PSS/GRAPHENE

To show that PAH and PSS on graphene surface act as positive and negative potential gating, Raman spectroscopy was employed to monitor the changes of G-band and its full width at half maximum (FWHM) value before and after deposition of the PEM. We first measured the Raman spectrum of clean graphene that was transfer printed onto SiO_2 by PDMS. Then the polyelectrolyte films PAH or PSS were deposited on the graphene surface. Figures 4.2.(a) and (b) present the Raman spectra of the G band before and after adsorbing the polyelectrolyte film PAH or PSS. After PAH coating, the average position of G band has a blue shift about 3.1 cm^{-1}

while the FWHM value of G band decreases by 3.2 cm^{-1}. This blue shift and FWHM reduction are caused by the positively charged PAH and due to stiffening of G band for non-adiabatic Kohn-anomaly[84,85]. For the PSS coating, the G band is shifted to right about 4.2 cm^{-1} while the FWHM value reduces by 3.4 cm^{-1}. These changes are generated by the negatively charged PSS film due to stiffening of the G band according to the adiabatic Born-Oppenheimer approximation[84]. The observations of the blue shift of the G band and the reduction of FWHM values for absorbing positively charged PAH and negatively charged PSS on graphene surface are both in agreement with previously obtained results for electrostatic gating[85-87].

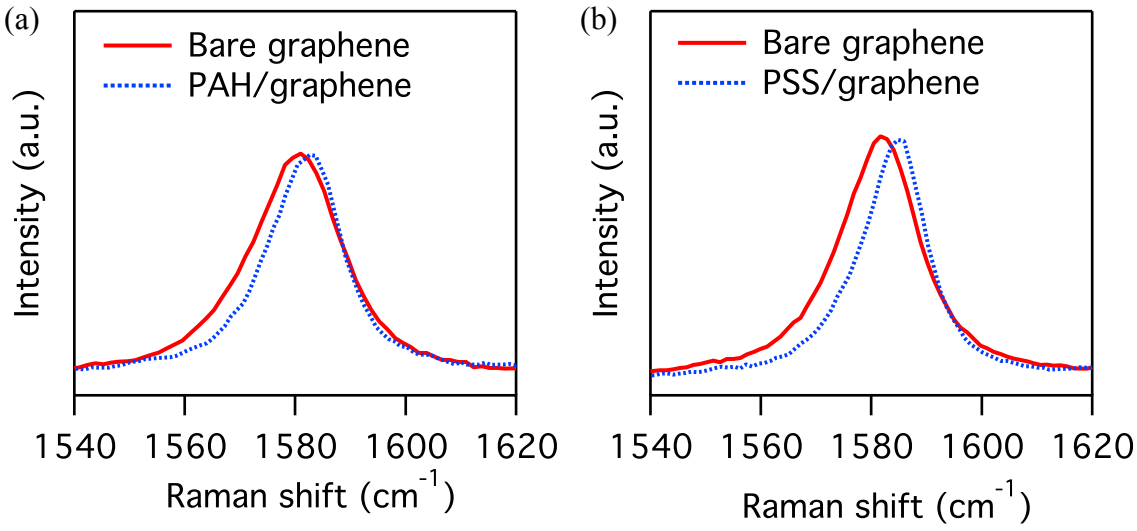

Figure 4.2. Raman spectra of G peak position and FWHM values for single layer graphene before and after coating polyelectrolyte film (a) PAH and (b) PSS.

4.3.3. FTIR SPECTRA OF GRAPHENE, PAH/GRAPHENE AND PSS/GRAPHENE

In order to confirm the expected composition of the polyelectrolyte multilayer, FTIR was employed on samples made for this project. Figure 4.3. shows the FTIR spectra of bare graphene, PAH/graphene and PSS/graphene films on calcium fluoride substrates. The bare graphene shows no adsorption in the FTIR spectrum. For the PAH/graphene film, the band around 3,330 cm^{-1} is attributed to the NH_3^+ group. In the PSS/graphene film, the band around 1,190 cm^{-1} is due to the SO_3^- group. The FTIR spectra confirm the presence of PAH and PSS polyelectrolyte films on the graphene surface, as expected.

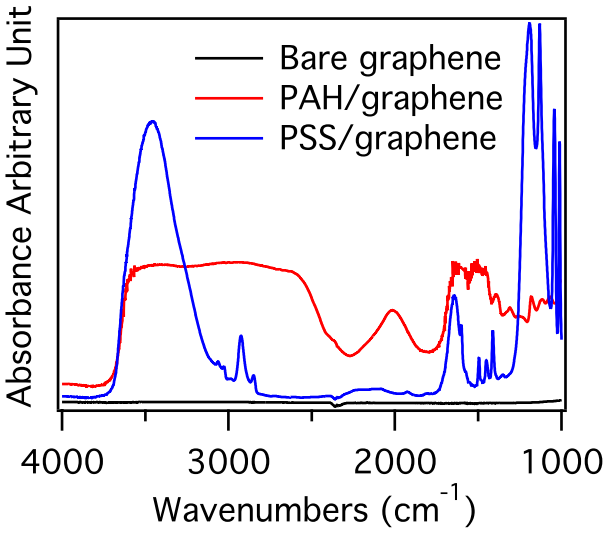

Figure 4.3. FTIR spectra of bare graphene, PAH/graphene and PSS/graphene films on calcium fluoride substrates.

4.3.4. THICKNESS MEASUREMENT OF PAH AND PSS

To measure the thickness of PAH and PSS films on the surface of graphene, ellipsometry was employed. The CVD-grown graphene was transferred onto a Si wafer using PMMA transfer.

After PMMA was cleaned by acetone, the graphene sample was annealed in H2 /Ar (50%/50%) at 400 ° C for 1 h. Then the PAH and PSS films were deposited on the graphene surface by the same process described in the main article. The average thickness is about 1.2 nm for both PAH and PSS films on the surface of graphene.

4.4. DISCUSSION

In order to develop an electrostatic model, we first discuss the results for a single layer of PAH or PSS on graphene. Figure 4.4. presents the transfer characteristics of graphene FETs for bare graphene, PAH/graphene and PSS/graphene in (a) 1 and (b) 100 mM NaCl at V_{ds} = 0.1 V. The Dirac point of bare graphene is at 90 mV at 1 mM (Fig. 4.4.(a)) and 10 mV at 100 mM (Fig. 4.4.(b)). This residual background doping is presumably due to substrate impurities and is consistent with similar work in the literature. After the positively charged polyelectrolyte film PAH is deposited on the graphene surface, the Dirac point shifts to a more negative gate voltage. Similarly, after the negatively charged polyelectrolyte film PSS is deposited on the graphene surface, the Dirac point shifts to a more positive gate voltage. We also found the magnitude of the Dirac voltage shift can be controlled by adjusting the adsorption concentrations (the change of Dirac point is proportional to the concentration of PAH and PSS). Precise control of the Dirac point shift requires control of both the concentration and thickness (see model below); control of one parameter alone does not guarantee consistent tunability. The ability to controllably shift the Dirac point opens up more opportunities for applications. We now describe this effect in terms of a simple electrostatic gating model.

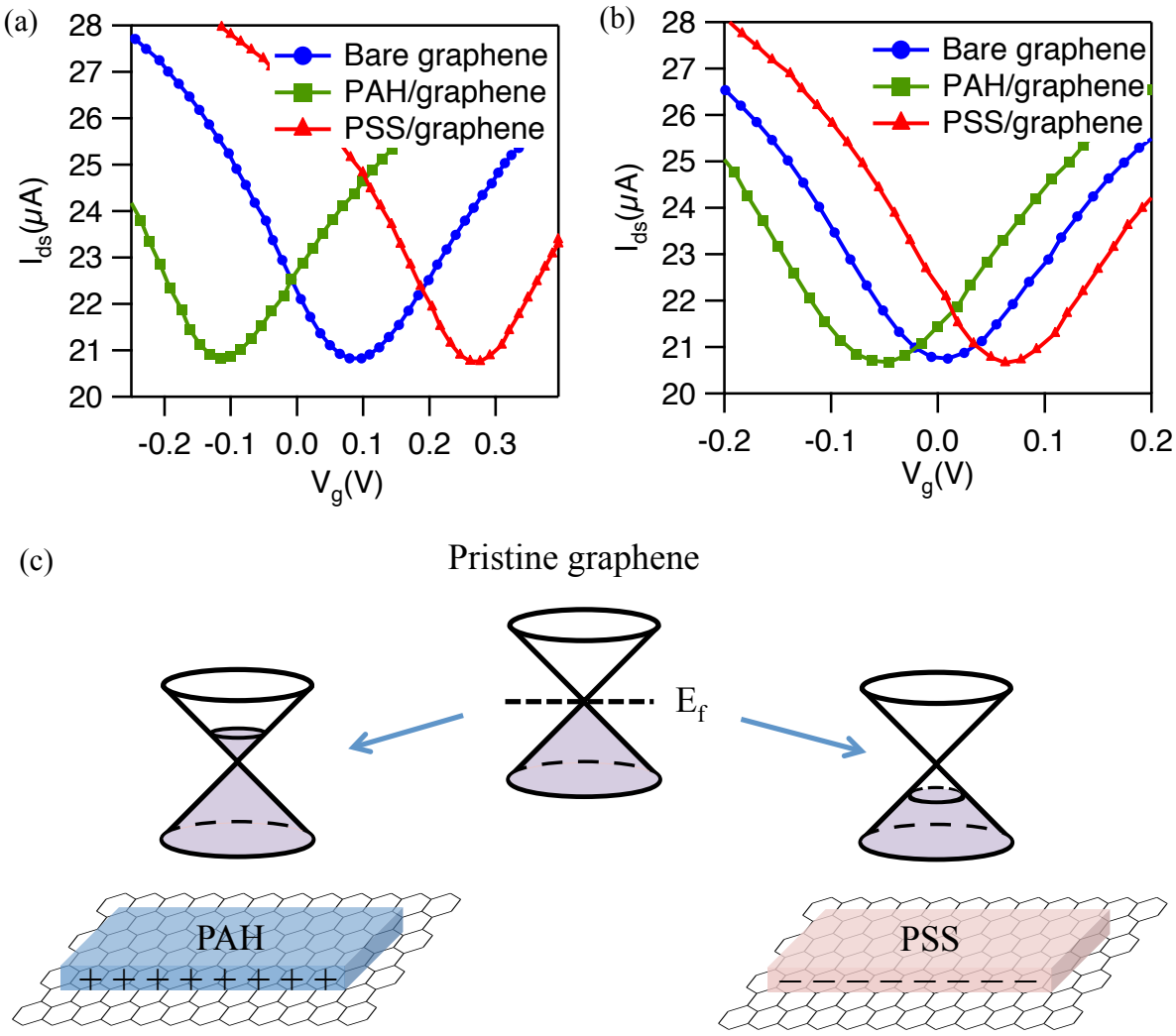

Figure 4.4. Transfer characteristic of graphene FETs for bare graphene, PAH/graphene and PSS/graphene in (a) 1 mM and (b) 100 mM NaCl at V_{ds} = 0.1 V. (c) The relationship between the Fermi energy shift and the deposition of PAH and PSS on the graphene surface.

In figure 4.5., we present a simple electrostatic model explaining the interaction between the charged polymer and the electrolyte which accounts for our observed Dirac voltage shifts. Figures 4.5.(a)–(c) depict a capacitor equivalent circuit model (a), the classical example

(provided for a well-studied comparison to graphene) of an electrolyte in contact with a metal with no specifically adsorbed species (b), and the analogous case of graphene in contact with an electrolyte (c). Application of a positive potential to an electrolyte in contact with a classic metal induces a negative charge on the metal (figure 4.5.(b)), balanced by a positive layer of charged cations adsorbed to the surface of the metal (the double layer). An analogous situation occurs when the electrode is a graphene electrode (figure 4.5.(c)). In the case of graphene, the induced negative charge on the graphene shifts the Fermi energy into the conduction band. Key assumeptions in this model are that (1) there are no redox reactions between the electrolyte and the electrode; (2) at zero applied bias to the electrolyte, there are no specifically adsorbed charges species on the surface of the metal (figure 4.5.(b)) or graphene (figure 4.5.(c)) electrode; (3) there is no charge transfer from the adsorbed ions to the graphene (figure 4.5.(c)). We will revisit these key assumptions (which differentiate this work from analogous work on silicon, silicon nanowires, and carbon nanotubes) later in the paper. For now, we will make the case that this explains the effect of the PAH on graphene in a simple way.

We next consider what happens when a positively charged PAH is deposited onto a solid surface. Two possible scenarios emerge. The first is that the positive charges are complemented by negatively charged anions in solution inside the PAH, resulting in a net zero charge density. This happens if the layer thickness is large compared to the Debye screening length. The second is that the charges are not compensated, and that there is a net positive charge density. Although there is not universal agreement on this, it is generally believed that the latter case (uncompensated charges) occurs when the layer thickness is less than the Debye screening length[88,89]. Simply put, the positive charges of the PAH are not shielded and leave a net positive

charge density on top of the electrode. We now consider the effects of this on the electrostatic gating effect.

The positively charged PAH attracts a layer of negatively charged adsorbed anions on the surface. In addition, the positively charged PAH layers induces a negative charge on the surface of the metal figure 4.5.(e) or graphene figure 4.5.(f). The three charges (the double layer charge Q_{DL}, the PAH charged which is fixed Q_{Fixed} , and the induced charge $Q_{Induced}$) are not necessarily equal; only Q_{Fixed} remains independent of the bias voltage. Even at zero applied bias, all three charges are not necessarily zero. As the bias voltage on the Ag/AgCl electrode is reduced further to become negative, the induced charge on the metal figure 4.5.(e) or graphene figure 4.5.(f) electrodes is reduced and eventually becomes zero. In this case, the double layer charge Q_{DL} exactly balances the fixed PAH charge Q_{Fixed}, and the induced charge density on the metal figure 4.5.(h) or graphene figure 4.5.(i) is zero. This corresponds to the Dirac point of graphene. The double layer capacitance can be modeled[90] as $C_{DL}= A\kappa_d\varepsilon_d\varepsilon_o$, where A is area, k_d is the Debye screening length, ε_d is the relative dielectric constant in water, and $\varepsilon_o = 8.85 \times 10^{-12}$ F/m. In this model, the Dirac voltage will shift by

$$\Delta V_{Dirac} = -Q_{Fixed}/C_{DL}= -\sigma/\kappa_d\varepsilon_d\varepsilon_o \quad (1),$$

where σ is the polymer areal charge density. Similarly, if the polymer is negatively charged, the Dirac voltage will shift in the opposite direction. As the double layer capacitance depends on the screening length, which in turn depends on the electrolyte molarity, this predicts a different Dirac voltage shift depending on the KCl concentration.

This model explains quantitatively the features we observe when a single layer of positively (PAH) or negatively (PSS) charged polymer is deposited on the graphene surface: The voltage shift is positive or negative, as expected from the model figure 4.5.(a),(b). In addition, the magnitude of the voltage shift is larger at smaller NaCl concentrations, consistent with the model: At smaller NaCl concentrations, the Debye screening length is larger, hence the double layer capacitance is smaller, and hence the Dirac voltage shift is larger, as per eq. (1). Using an estimated value of 7.2 and 72 mF/cm^2 at 1 and 100 mM NaCl[90], and the measured Dirac voltage shift of 0.18 and 0.06 V respectively, yields values of s of 0.013 and 0.043 C/m^2, for the polymer surface charge density, consistent with reported literature values for PEMs deposited under similar conditions[91].

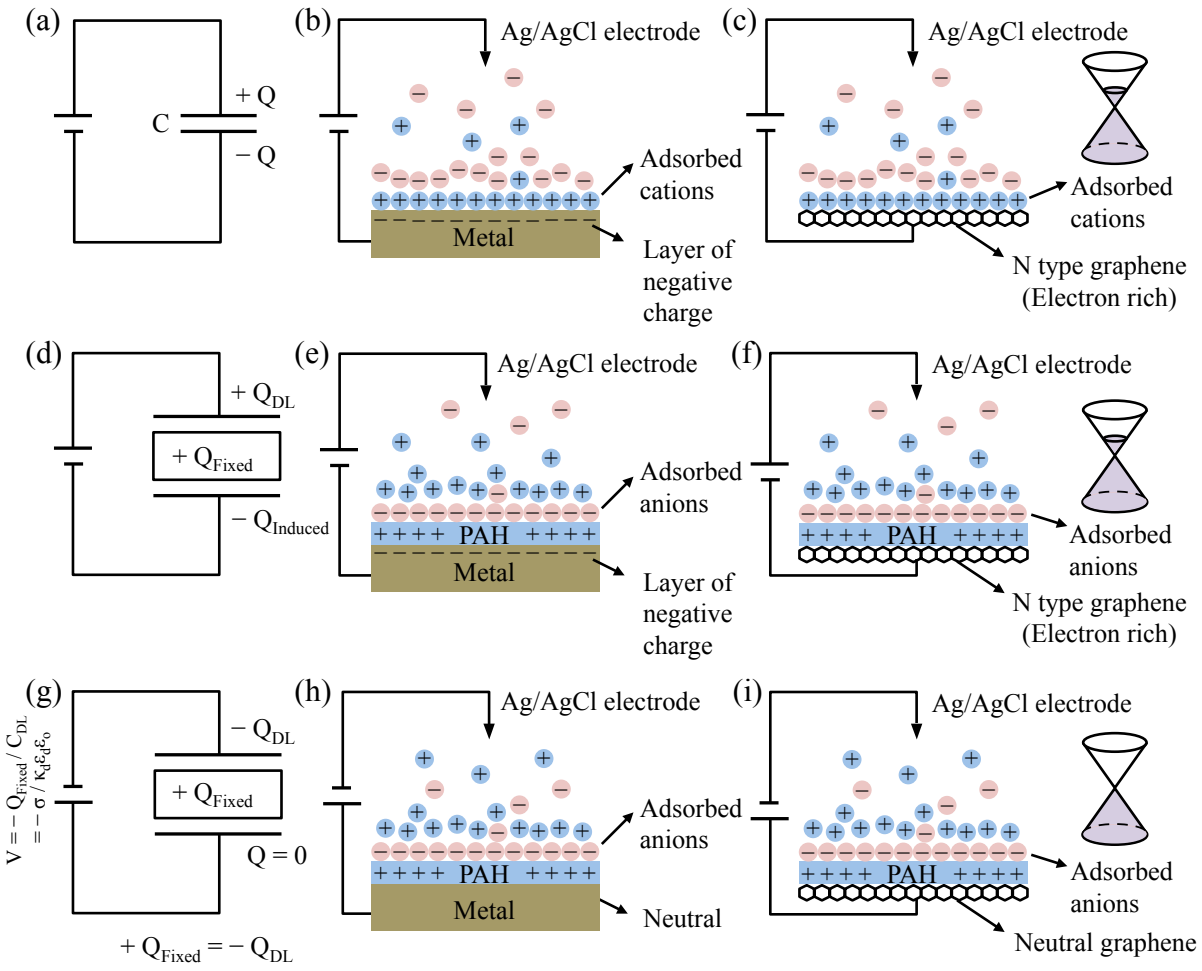

Figure 4.5. Explanation of electrostatic gating model of PAH on graphene. In the top row, for comparison, we show (a) the circuit model for an electrolyte in contact with an electrode, (b) the buildup of charge at a metal electrode in reponse to an applied voltage on the electrolyte, and (c) the analogous case for graphene in contact with an electrolyte. In the second row, we present the modification to the electrostatics when (d) a fixed charge is placed in between the capacitor plates, (e) a fixed charge of finite thickness is deposited on a metal in the presence of an electrolyte, and (f) a fixed charge of finite thickness is deposted on the surface of graphene. In the bottom row, we present the special case of a negative applied voltage that exactly cancels the induced charge. In circuit terms, (g), at a specific applied voltage, the fixed charge exactly

balances the double layer, (h) the induced charge on the metal is zero, and (i) the graphene charge is zero, i.e. the Dirac voltage is shifted from zero to Q_{Fixed}/C_{DL}, where C_{DL} is the double layer capacitance, $A\kappa_d\varepsilon_d\varepsilon_o$. (Symbols defined in text.)

In our next series of experiments, we sequentially deposited positively charged polymer PAH and negatively charged polymer PSS on graphene FETs for up to six layers, and measured the shift in the Dirac voltage in response to each layer. Figure 4.6. shows the transfer characteristics of graphene FETs as a function of PAH/PSS multilayers measured in (a) 1 mM NaCl and (b) 100 mM NaCl. The Dirac voltage shifts back and forth in response to addition of each layer, with almost no Dirac voltage shift at even layer numbers (i.e. the total deposited charge is zero). A simple model to explain this shift is based on alternating layers of positive and negative charges. From the basic model presented for a single layer, we expect that if an even number of layers is present, they will cancel (the net fixed charged will be zero), and the Dirac voltage will shift back to the original position. This is indeed what we observe experimentally. If the number of layers is odd, the net charged will be positive. The negative gate voltage will be required to balance it in order to observe the Dirac point.

If the number of layers becomes sufficiently large, then the total thickness will exceed the Debye screening length. In that case, the simple model presented above will no longer apply, and a more sophisticated model which takes into account the finite screening length needs to be developed. Briefly, the fixed PEM charges will be screened and a solution for the spatial profile of the potential needs to be developed. Such a model was presented in Ref.[91], and gives rise to the following prediction for the shift in the Dirac voltage with layer number

$\Delta V_{Dirac}(N) = \sigma/C_D[(C_p/C_D)\sinh(\kappa_p Nd) + \cosh(\kappa_p Nd)]$ (2) ,

where $C_p = \kappa_p \varepsilon_p \varepsilon_o$ and $C_D = \kappa_d \varepsilon_d \varepsilon_o$ are the capacitances (per area) for polymer multilayer and electrolyte solution, κ_p and κ_d are the Debye lengths of polymer film and electrolyte solution[92], ε_p and ε_d are the dielectric constant for polymer film and electrolyte solution[91,92], the number of polymer layers is N, the thickness of each layer is d[92], and s is the polymer layer's surface charge density. In our case, the parameter $\kappa_p Nd$ is less than one (0.05), so the dependence on N is mild and the simple model we presented above is actually quite close to the experimental data, as expected.

Taken collectively, our experiments indicate that electrostatic gating by charged polymers can dominate the Dirac voltage shift, which is a different mechanism from the sensing mechanism for the first two classes of sensing introduced in the beginning of this paper, which involves ionization of dangling bonds of residual organic impurities from the processing, ionization of dangling bonds in the graphene itself, or specific adsorption of OH^- or H^+, or shielding of these charges. This work demonstrates a clear and simple canonical example of sensing of charged polymers by graphene.

We now compare this work to similar work on silicon on insulators, silicon oxide, silicon nanowires, and carbon nanotubes, each with a qualitatively different set of electrostatic and chemical properties, quite distinct from graphene. The history of polymer electrolytes on silicon and silicon oxide (which is charged and ionizable in a way that directly affects quantum transport, doping, and gating electrostatics) is very mature, and its effects have been applied in

silicon nanowire biosensors. The work presented here follows that of Neff on silicon on insulator planar devices[91], where the surface presents an electrostatic potential sensitive conductance. However, the difference with graphene is that it is putatively non-reactive, with fewer dangling bonds. In contrast, the work of Neff, as well as other subsequent work using silicon nanowires[93,94], relied heavily on the more reactive silanol groups for the sensing mechanism. This has both advantages and disadvantages, the most significant advantage being the ability to covalently functionalize the surface with different moieties. Carbon nanotubes were also investigated using this technique by Noy[95]. There, the dominant sensing mechanism was changed in the substrate (NOT the nanotube) electrostatics, which indirectly affected the nanotube conductance via local gating effects. In that work, the mechanism of electrostatic gating effects was more complicated because the single carbon nanotube is affected by the polyelectrolyte multilayer as well as the silicon oxide substrate, with ionizable side groups that change the electrostatics in the vicinity of the nanotube.

During the preparation of this manuscript, a similar paper was published using a solvent n-type doping[96]. Our work is complementary, in that we study charged polymers (rather then small molecules), and our polymers can be both positively or negatively charged, allowing a more thorough investigation of the gating mechanism, as well as the ability to create both n-type or p-type graphene at will. In addition, in contrast to Ref.[96], our approach can in principle be extended to dry (solvent free) operation.

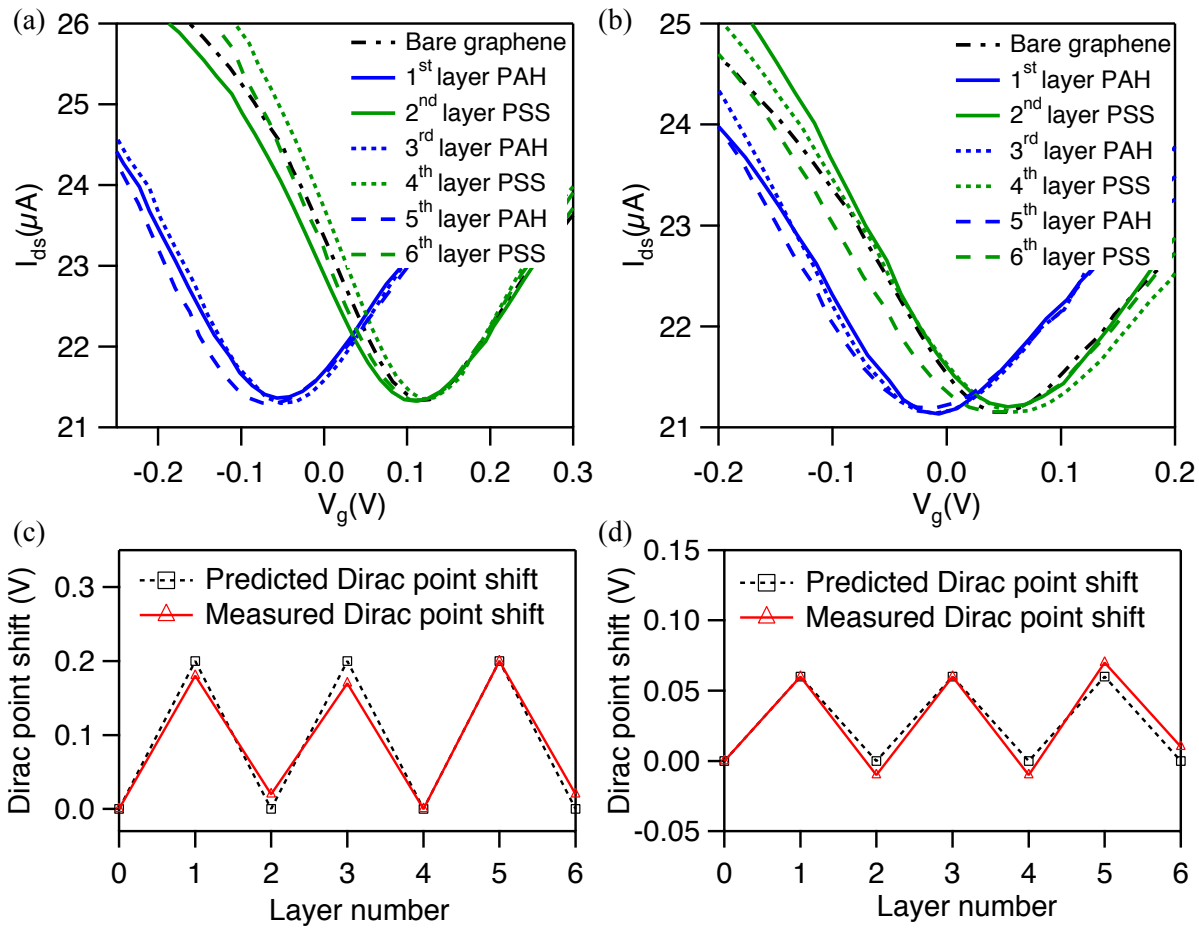

Figure 4.6. Transfer characteristics of graphene FET devices as a function of # of PAH/PSS multilayers measured in (a) 1 mM NaCl and (b) 100 mM NaCl at V_{ds} = 0.1V. Transfer characteristics of the device before (black dash and dot line) and after polymer coating with PAH (blue lines) and PSS (green lines). 1st and 2nd layers are solid lines. 3rd and 4th layers are dot lines. 5th and 6th layers are dash lines. Measured (red triangles) and predicted (black squares) device Dirac point voltage shift *vs*. the number of coating polymer layers for (c) 1 mM NaCl and (d) 100 mM NaCl. The Dirac point voltage of the uncoated device is regarded as reference point.

4.5. CONCLUSION

We have demonstrated an electrostatic gating effect on graphene FETs using a simple, well known charged polymer system. We observed the shift of the Dirac point while depositing positively charged polymer PAH and negatively charged polymer PSS. A simple electrostatic model accounts well for the sign and magnitude of the Dirac voltage shift. Using this simple system, we are able to create p-type or n-type graphene at will. This model serves as the basis for understanding the mechanism of charged polymer sensing using graphene devices, a potentially technologically important application of graphene in areas such as DNA sequencing, biomarker assays for cancer detection, and other protein sensing applications.

CHAPTER FIVE

SUMMARY AND CONCLUSION

5.1. SUMMARY OF FINDINGS AND CONCLUSION

In conclusion, we have introduced a simple, large area, low-cost and contamination-free method to transfer CVD-grown graphene on PDMS substrates. Then monolayer graphene field-effect transistor can be fabricated directly on PDMS substrates. The advantages of this device are not only preventing the mobility degradation of annealing process on the graphene film but also avoiding the contamination of photoresists. Other advantages of this device are large area and contamination-free clean monolayer graphene surface. This device can be a good platform to study the effects of chemical and biological materials in liquid-gated ambipolar characteristics. The effects of graphene's Dirac point with different etching solution and concentrations are investigated. In addition, the devices have shown the liquid-gated sensing applications for different KCl concentrations and pH values. The result is committed that this device has great potential for chemical and biological liquid-gated sensor applications.

In our second project, we have demonstrated the single layer of graphene FETs combined with SLBs for different sensing applications. The fluorescence image showed the graphene surface is covered by intact supported lipid bilayers that provide a seal on graphene FETs. With SLBs coating, the graphene FETs are not sensitive to different KCl concentration and different pH solution. Finally, the single ion channel activity of alamethicin and gramicidin A is recorded by graphene-supported lipid bilayers biosensors. The different voltage is applied to observe the effect of different ion channel with SLBs on the graphene surface. This biosensor has many potential applications in the study of detection of individual molecules and monitoring biochemical reactions at a single-molecule level. This device can also serve as platform for

studies of the physical, electrical and optical interaction of single molecules with CVD-grown graphene.

In the last project, the electrostatic gating effect on graphene FETs are observed by the shift of Dirac point while depositing positively charged polymer PAH and negatively charged polymer PSS. The scanning electron microscopy, Raman spectroscopy and Fourier transform infrared spectroscopy are employed to characterize polyelectrolyte films on graphene surface. We are able to control the Dirac point of graphene to present regular oscillations with sequential adsorption of positively and negatively charged polymer electrolytes. The periodic behavior of the Dirac point is well described by a simple electrostatic model. Our work provides a comprehensive understanding of the electrostatic gating effect on graphene FETs important for any chemical and biological sensing applications that rely on electrostatic gating, which includes a large class of charged species such as DNA and sequencing, biomarker assays for cancer detection and other protein sensing applications.

5.2. ACKNOWLEDGMENTS

The first work was funded by the Army Research Office through ARO-MURI program and ARO-Core grants (MURI W911NF-11-1-0024, ARO W911NF-09-1-0319, and DURIP W911NF-11-1-0315).

We thank James Hall, Bruce Cornell, and Jan Behrends for insightful discussions about our data prior to publication. This second work was funded by the Army Research Office through ARO-MURI program and ARO-Core grants (MURI W911NF-11-1-0024, ARO W911NF-09-1-

0319, and DURIP W911NF-11-1-0315), and from an NIH National Cancer Institute Grant 1R21CA143351-01.

The third work was fund by the Army Research Office through the ARO-MURI program and ARO-Core grants (Nos. MURI W911NF-11-1-0024, ARO W911NF- 09-1-0319, and DURIP W911NF-11-1-0315) and NIH grant (No. 1R21CA143351-01).

5.3. REFERENCES

[1] Allen, M.J., Tung, V.C. & Kaner, R.B. Honeycomb carbon: a review of graphene. *Chemical reviews*. **2010**, 110, 132-45.

[2] Chen, J.-H.H., Jang, C., Xiao, S., Ishigami, M. & Fuhrer, M.S. Intrinsic and extrinsic performance limits of graphene devices on SiO2. *Nat Nano*. **2008**, 3, 206-209.

[3] Akturk, A. & Goldsman, N. Electron transport and full-band electron-phonon interactions in graphene. *Journal of Applied Physics.* **2008**, 103, 053702.

[4] Novoselov, K.S. *et al.* Electric field effect in atomically thin carbon films. *Science (New York, N.Y.).* **2004**, 306, 666-9.

[5] Magnetic, H. Epitaxial graphene. *Solid State Communications* 1-19.

[6] Dong, X., Shi, Y., Huang, W., Chen, P. & Li, L.-J. Electrical detection of DNA hybridization with single-base specificity using transistors based on CVD-grown graphene sheets. *Advanced materials (Deerfield Beach, Fla.).* **2010***,* 22, 1649-53.

[7] Reina, A. *et al.* Large area, few-layer graphene films on arbitrary substrates by chemical vapor deposition. *Nano letters.* **2009***,* 9, 30-5.

[8] Reina, A. *et al.* Growth of large-area single- and Bi-layer graphene by controlled carbon precipitation on polycrystalline Ni surfaces. *Nano Research.* **2010**, 2, 509-516.

[9] Li, X. *et al.* Large-area synthesis of high-quality and uniform graphene films on copper foils. *Science (New York, N.Y.)*. **2009**, 324, 1312-4.

[10] Geim, A. K. Graphene: status and prospects. *Science*. **2009**, *324*, 1530–1534.

[11] Novoselov, K. S.; Fal'ko, V. I.; Colombo, L.; Gellert, P. R.; Schwab, M. G.; Kim, K. A Roadmap for graphene. *Nature* **2012**, *490*, 192–200.

[12] Ang, P. K.; Chen, W.; Wee, A. T. S.; Loh, K. P. Solution-gated epitaxial graphene as pH sensor. *J. Am. Chem. Soc*. **2008**, *130*, 14392–14393.

[13] Ohno, Y.; Maehashi, K.; Yamashiro, Y.; Matsumoto, K. Electrolyte-gated graphene field-effect transistors for detecting pH and protein adsorption. *Nano Lett*. **2009**, *9*, 3318–3322.

[14] Yu, Q.; Lian, J.; Siriponglert, S.; Li, H.; Chen, Y. P.; Pei, S. S. Graphene segregated on Ni surfaces and transferred to insulators. *Appl. Phys. Lett*. **2008**, *93*, 113103.

[15] Li, X.; Cai, W.; An, J.; Kim, S.; Nah, J.; Yang, D.; Piner, R.; Velamakanni, A.; Jung, I.; Tutuc, E.; et al. Large-Area Synthesis of high-quality and uniform graphene films on copper foils. *Sci*. **2009**, *324* , 1312–1314.

[16] Dan, Y.; Lu, Y.; Kybert, N. J.; Luo, Z.; Johnson, A. T. C. Intrinsic response of graphene vapor sensors. *Nano Lett*. **2009**, *9*, 1472–1475.

[17] Geringer, V.; Subramaniam, D.; Michel, A. K.; Szafranek, B.; Schall, D.; Georgi, A.; Mashoff, T.; Neumaier, D.; Liebmann, M.; Morgenstern, M. Electrical Transport and low-temperature scanning tunneling microscopy of microsoldered graphene. *Appl. Phys. Lett*. **2010**, *96*, 82114.

[18] Pirkle, A.; Chan, J.; Venugopal, A.; Hinojos, D.; Magnuson, C. W.; McDonnell, S.; Colombo, L.; Vogel, E. M.; Ruoff, R. S.; Wallace, R. M. The effect of chemical residues on the physical and electrical properties of chemical vapor deposited graphene transferred to SiO_2. *Appl. Phys. Lett.* **2011**, *99*, 122108.

[19] Chen, S.; Cai, W.; Chen, D.; Ren, Y.; Li, X.; Zhu, Y.; Kang, J.; Ruoff, R. S. Adsorption/desorption and electrically controlled flipping of ammonia molecules on graphene. *New J. Phys.* **2010**, *12*, 125011.

[20] Cheng, Z.; Zhou, Q.; Wang, C.; Li, Q.; Wang, C.; Fang, Y. Toward intrinsic graphene surfaces: a systematic study on thermal annealing and wet-chemical treatment of SiO_2-supported graphene devices. *Nano Lett.* **2011**, *11*, 767–771.

[21] Li, X.; Cai, W.; Jung, I. H.; An, J. H.; Yang, D.; Velamakanni, A.; Piner, R.; Colombo, L.; Ruoff, R. S. Synthesis, characterization, and properties of large-area graphene films. *ECS Trans.* **2009**, *19* , 41–52.

[22] Allen, M. J.; Tung, V. C.; Gomez, L.; Xu, Z.; Chen, L.-M.; Nelson, K. S.; Zhou, C.; Kaner, R. B.; Yang, Y. Soft transfer printing of chemically converted graphene. *Adv. Mater.* **2009**, *21*, 2098–2102.

[23] Kim, K. S.; Zhao, Y.; Jang, H.; Lee, S. Y.; Kim, J. M.; Kim, K. S.; Ahn, J.-H.; Kim, P.; Choi, J.-Y.; Hong, B. H. Large-scale pattern growth of graphene films for stretchable transparent electrodes. *Nature* **2009**, *457*, 706–710.

[24] Lee, Y.; Bae, S.; Jang, H.; Jang, S.; Zhu, S.-E.; Sim, S. H.; Song, Y. Il; Hong, B. H.; Ahn, J.-H. Wafer-scale synthesis and transfer of graphene films. *Nano Lett.* **2010**, *10*, 490–493.

[25] Oznuluer, T.; Pince, E.; Polat, E. O.; Balci, O.; Salihoglu, O.; Kocabas, C. Synthesis of graphene on gold. *Appl. Phys. Lett.* **2011**, *98*, 183101–183103.

[26] Kang, S. J.; Kim, B.; Kim, K. S.; Zhao, Y.; Chen, Z.; Lee, G. H.; Hone, J.; Kim, P.; Nuckolls, C. Inking Elastomeric stamps with micro-patterned, single layer graphene to create high-performance OFETs. *Adv. Mater.* **2011**, *23*, 3531–3535.

[27] Su, C. Y.; Fu, D.; Lu, A. Y.; Liu, K. K.; Xu, Y.; Juang, Z. Y.; Li, L. J. Transfer printing of graphene strip from the graphene grown on copper wires. *Nanotechnology* **2011**, *22*, 185309.

[28] Song, J.; Kam, F.-Y.; Png, R.-Q.; Seah, W.-L.; Zhuo, J.-M.; Lim, G.-K.; Ho, P. K. H.; Chua, L.-L. A General method for transferring graphene onto soft surfaces. *Nat Nano* **2013**, *8*, 356–362.

[29] See supplementary material at http://dx.doi.org/10.1063/1.4816764 for optical image of monolayer graphene on PDMS substrate (Figure 1.5.), Raman spectra of PDMS and graphene/PDMS (Figure 1.6.), leakage current of graphene FET (Figure 1.7.), contact resistance of silver paste on graphene sheet (Figure 1.8.), and AFM topographic images of PMMA/graphene film (Figure 1.9.).

[30] Graf, D.; Molitor, F.; Ensslin, K.; Stampfer, C.; Jungen, A.; Hierold, C.; Wirtz, L. Spatially resolved Raman spectroscopy of single- and few-layer graphene. *Nano Lett.* **2007**, *7*, 238–242.

[31] Rouhi, N.; Capdevila, S.; Jain, D.; Zand, K.; Wang, Y.; Brown, E.; Jofre, L.; Burke, P. Terahertz graphene optics. *Nano Res.* **2012**, *5*, 667–678 LA – English.

[32] Docherty, C. J.; Lin, C. T.; Joyce, H. J.; Nicholas, R. J.; Herz, L. M.; Li, L. J.; Johnston, M. B. Extreme sensitivity of graphene photoconductivity to environmental gases. *Nat. Commun.* **2012**, *3*, 1228.

[33] Parrish, K. N.; Akinwande, D. Impact of contact resistance on the transconductance and linearity of graphene transistors. *Appl. Phys. Lett.* **2011**, *98*, 183505.

[34] Heller, I.; Chatoor, S.; Männik, J.; Zevenbergen, M. A. G.; Dekker, C.; Lemay, S. G. Influence of electrolyte composition on liquid-gated carbon nanotube and graphene transistors. *J. Am. Chem. Soc.* **2010**, *132*, 17149–17156.

[35] Chen, F.; Qing, Q.; Xia, J.; Li, J.; Tao, N. Electrochemical gate-controlled charge transport in graphene in ionic liquid and aqueous solution. *J. Am. Chem. Soc.* **2009**, *131*, 9908–9909.

[36] Artyukhin, A. B.; Stadermann, M.; Friddle, R. W.; Stroeve, P.; Bakajin, O.; Noy, A. controlled electrostatic gating of carbon nanotube FET devices. *Nano Lett.* **2006**, *6*, 2080–2085.

[37] Guidelli, R.; Becucci, L. Model Lipid Bilayers at Electrode Surfaces. In *Advances in Electrochemical Science and Engineering*; Wiley-VCH Verlag GmbH & Co. KGaA, 2011; pp. 189–227.

[38] Cornell, B. A.; Braach-Maksvytis, V. L. B.; King, L. G.; Osman, P. D. J.; Raguse, B.; Wieczorek, L.; Pace, R. J. A Biosensor That Uses Ion-Channel Switches. *Nature* **1997**, *387*, 580–583.

[39] Krishnamurthy, V.; Cornell, B. Engineering Aspects of Biological Ion Channels—from Biosensors to Computational Models for Permeation. *Protoplasma* **2012**, *249*, 3–9.

[40] Bayley, H.; Cremer, P. S. Stochastic Sensors Inspired by Biology. *Nature* **2001**, *413*, 226–230.

[41] Novoselov, K. S.; Fal'ko, V. I.; Colombo, L.; Gellert, P. R.; Schwab, M. G.; Kim, K. A Roadmap for Graphene. *Nature* **2012**, *490*, 192–200.

[42] Xia, J.; Chen, F.; Li, J.; Tao, N. Measurement of the Quantum Capacitance of Graphene. *Nat. Nanotechnol.* **2009**, *4*, 505–509.

[43] Lim, T.-S.; Jain, D.; Burke, P. J. Fabrication of Supported Lipid Bilayer (SLB) and Nanotube Transistor Hybrid Biosensing Platform Using Microfluidic Channels. *Proc. 11th IEEE Conf. Nanotechnol.* **2011**, 371–373.

[44] Lim, T.-S.; Jain, D.; Burke, P. Biomembrane-Gated Carbon Nanotube Transistor as a Sensing Platform. *Proc. 15th Int. Conf. Miniaturized Syst. Chem. Life Sci.* **2011**, 1770–1772.

[45] Lim, T.-S.; Jain, D.; Burke, P. J. Protein Nanopore-Gated Bio-Transistor for Membrane Ionic Current Recording. *Proc. 69th Device Res. Conf.* **2011**, *26*, 131–132.

[46] Alivisatos, A. P.; Andrews, A. M.; Boyden, E. S.; Chun, M.; Church, G. M.; Deisseroth, K.; Donoghue, J. P.; Fraser, S. E.; Lippincott-Schwartz, J.; Looger, L. L.; et al. Nanotools for Neuroscience and Brain Activity Mapping. *ACS Nano* **2013**, *7*, 1850–1866.

[47] Alivisatos, A. P.; Chun, M.; Church, G.; Deisseroth, K.; Donoghue, J. P.; Greenspan, R. J.; McEuen, P. L.; Roukes, M. L.; Sejnowski, T. J.; Weiss, P. S.; et al. The Brain Activity Map. *Science*. **2013**, *339*, 1284–1285.

[48] Kralj, J. M.; Hochbaum, D. R.; Douglass, A. D.; Cohen, A. E. Electrical Spiking in Escherichia Coli Probed with a Fluorescent Voltage-Indicating Protein. Science. 2011, 333, 345–348.

[49] Wang, Y. Y.; Burke, P. J. A Large-Area and Contamination-Free Graphene Transistor for Liquid-Gated Sensing Applications. *Appl. Phys. Lett.* **2013**, *103*, 052103.

[36] Freeman, L. M.; Li, S.; Dayani, Y.; Choi, H.-S.; Malmstadt, N.; Armani, A. M. Excitation of Cy5 in Self-assembled Lipid Bilayers Using Optical Microresonators. *Appl. Phys. Lett.* **2011**, *98*, 143703.

[51] Nirasay, S.; Badia, A.; Leclair, G.; Claverie, J.; Marcotte, I. Polydopamine-Supported Lipid Bilayers. *Materials.* **2012**, *5*, 2621–2636.

[52] Luryi, S. Quantum Capacitance Devices. *Appl. Phys. Lett.* **1988**, *52*, 501–503.

[53] Bard, A. J.; Faulkner, L. R. *Electrochemical Methods : Fundamentals and Applications*; 2nd ed.; Wiley: New York, 1980; p. 833.

[54] Krishna, G.; Schulte, J.; Cornell, B. A.; Pace, R.; Wieczorek, L.; Osman, P. D. Tethered Bilayer Membranes Containing Ionic Reservoirs : The Interfacial Capacitance. *Langmuir* **2001**, *17*, 4858–4866.

[55] Krishnamurthy, V.; Monfared, S. M.; Cornell, B. Ion Channel Biosensors—Part II: Dynamic Modeling, Analysis, and Statistical Signal Processing. *IEEE Trans. Nanotechnol.* **2010**, *9*, 313–321.

[56] Andersson, M.; Keizer, H. M.; Zhu, C.; Fine, D.; Dodabalapur, A.; Duran, R. S. Detection of Single Ion Channel Activity on a Chip Using Tethered Bilayer Membranes. *Langmuir* **2007**, *23*, 2924–2927.

[57] Keizer, H. M.; Dorvel, B. R.; Andersson, M.; Fine, D.; Price, R. B.; Long, J. R.; Dodabalapur, A.; Köper, I.; Knoll, W.; Anderson, P. A. V; et al. Functional Ion Channels in Tethered Bilayer Membranes—Implications for Biosensors. *ChemBioChem* **2007**, *8*, 1246–1250.

[58] Andersson, M.; Okeyo, G.; Wilson, D.; Keizer, H.; Moe, P.; Blount, P.; Fine, D.; Dodabalapur, A.; Duran, R. S. Voltage-Induced Gating of the Mechanosensitive MscL Ion Channel Reconstituted in a Tethered Lipid Bilayer Membrane. *Biosens. Bioelectron.* **2008**, *23*, 919–923.

[59] Becucci, L.; D'Amico, M.; Cinotti, S.; Daniele, S.; Guidelli, R. Tethered Bilayer Lipid Micromembranes for Single-Channel Recording: The Role of Adsorbed and Partially Fused Lipid Vesicles. *Phys. Chem. Chem. Phys.* **2011**, *13*, 13341–13348.

[60] Becucci, L.; D'Amico, M.; Daniele, S.; Olivotto, M.; Pozzi, A.; Guidelli, R. A Metal-Supported Biomimetic Micromembrane Allowing the Recording of Single-Channel Activity and of Impedance Spectra of Membrane Proteins. *Bioelectrochemistry* **2010**, *78*, 176–180.

[61] Xia, J.; Chen, F.; Li, J.; Tao, N. Measurement of the Quantum Capacitance of Graphene. *Nat. Nanotechnol.* **2009**, *4*, 505–509.

[62] Li, W.; Tan, C.; Lowe, M. A.; Abruña, H. D.; Ralph, D. C. Electrochemistry of Individual Monolayer Graphene Sheets. *ACS Nano* **2011**, *5*, 2264–2270.

[63] Ang, P. K.; Jaiswal, M.; Lim, C. H. Y. X.; Wang, Y.; Sankaran, J.; Li, A.; Lim, C. T.; Wohland, T.; Barbaros, Ö.; Loh, K. P. A Bioelectronic Platform Using a Graphene-Lipid Bilayer Interface. *ACS Nano* **2010**, *4*, 7387–7394.

[64] Rafiee, J.; Mi, X.; Gullapalli, H.; Thomas, A. V.; Yavari, F.; Shi, Y.; Ajayan, P. M.; Koratkar, N. A. Wetting Transparency of Graphene. *Nat. Mater.* **2012**, *11*, 217–222.

[65] Shih, C.-J.; Wang, Q. H.; Lin, S.; Park, K.-C.; Jin, Z.; Strano, M. S.; Blankschtein, D. Breakdown in the Wetting Transparency of Graphene. *Phys. Rev. Lett.* **2012**, *109*, 176101.

[66] Guidelli, R.; Aloisi, G.; Becucci, L.; Dolfi, A.; Moncelli, M. R.; Buoninsegni, F. T. Bioelectrochemistry at Metal Water Interfaces. *J. Electroanal. Chem.* **2001**, *504*, 1–28.

[67] Vockenroth, I. K.; Atanasova, P. P.; Long, J. R.; Jenkins, A. T. A.; Knoll, W.; Köper, I. Functional Incorporation of the Pore Forming Segment of AChR M2 into Tethered Bilayer Lipid Membranes. *Biochim. Biophys. Acta* **2007**, *1768*, 1114–1120.

[68] Chen, F.; Qing, Q.; Xia, J.; Li, J.; Tao, N. Electrochemical Gate-Controlled Charge Transport in Graphene in Ionic Liquid and Aqueous Solution. *J. Am. Chem. Soc.* **2009**, *131*, 9908–9909.

[69] Heller, I.; Chatoor, S.; Männik, J.; Zevenbergen, M. A. G.; Dekker, C.; Lemay, S. G. Influence of Electrolyte Composition on Liquid-Gated Carbon Nanotube and Graphene Transistors. *J. Am. Chem. Soc.* **2010**, *132*, 17149–17156.

[70] Ohno, Y.; Maehashi, K.; Yamashiro, Y.; Matsumoto, K. Electrolyte-Gated Graphene Field-Effect Transistors for Detecting pH and Protein Adsorption. *Nano Lett*. **2009**, *9*, 3318–3322.

[71] Ang, P. K.; Chen, W.; Wee, A. T. S.; Loh, K. P. Solution-Gated Epitaxial Graphene as pH Sensor. *J. Am. Chem. Soc*. **2008**, *130*, 14392–14393.

[72] Kelkar, D. A.; Chattopadhyay, A. The Gramicidin Ion Channel: A Model Membrane Protein. *Biochim. Biophys. Acta* **2007**, *1768*, 2011–2025.

[73] Andrew Woolley, G.; Wallace, B. A. Model Ion Channels: Gramicidin and Alamethicin. *J. Membr. Biol*. **1992**, *129*, 109–136.

[74] Novoselov, K. S.; Fal'ko, V. I.; Colombo, L.; Gellert, P. R.; Schwab, M. G.; Kim, K. *Nature* **2012**, 490, 192–200.

[75] Dong, X.; Shi, Y.; Huang, W.; Chen, P.; Li, L. J. *Adv. Mater*. **2010**, 22, 1649–1653.

[76] Ohno, Y.; Maehashi, K.; Yamashiro, Y.; Matsumoto, K. *Nano Lett.* **2009**, 9, 3318–3322.

[77] Heller, I.; Chatoor, S.; Männik, J.; Zevenbergen, M. A. G.; Dekker, C.; Lemay, S. G. *J. Am. Chem. Soc.* **2010**, 132, 17149–17156.

[78] Ang, P. K.; Chen, W.; Wee, A. T. S.; Loh, K. P. *J. Am. Chem. Soc.* **2008**, 130, 14392–14393.

[79] Cole, D. J.; Ang, P. K.; Loh, K. P. *J. Phys. Chem. Lett*. **2011**, 2, 1799–1803.

[80] Mailly-Giacchetti, B.; Hsu, A.; Wang, H.; Vinciguerra, V.; Pappalardo, F.; Occhipinti, L.; Guidetti, E.; Coffa, S.; Kong, J.; Palacios, T. J. *Appl. Phys*. **2013**, 114, 084505.

[81] Rafiee, J.; Mi, X.; Gullapalli, H.; Thomas, A. V.; Yavari, F.; Shi, Y.; Ajayan, P. M.; Koratkar, N. A. *Nat. Mater*. **2012**, 11, 217–222.

[82] Fu, W.; Nef, C.; Knopfmacher, O.; Tarasov, A.; Weiss, M.; Calame, M.; Schönenberger, C. *Nano Lett.* **2011**, 11, 3597–3600.

[83] Chen, F.; Qing, Q.; Xia, J.; Li, J.; Tao, N. J. *Am. Chem. Soc.* **2009**, 131, 9908–9909.

[84] Lazzeri, M.; Mauri, F. *Phys. Rev. Lett*. **2006**, 97, 266407.

[85] Pisana, S.; Lazzeri, M.; Casiraghi, C.; Novoselov, K. S.; Geim, A. K.; Ferrari, A. C.; Mauri, F. *Nat. Mater*. **2007**, 6, 198–201.

[86] Yan, J.; Zhang, Y.; Kim, P.; Pinczuk, A. *Phys. Rev. Lett*. **2007**, 98, 166802–4.

[87] Das, A.; Pisana, S.; Chakraborty, B.; Piscanec, S.; Saha, S. K.; Waghmare, U. V.; Novoselov, K. S.; Krishnamurthy, H. R.; Geim, A. K.; Ferrari, A. C.; Sood, A.K. *Nat. Nanotechnol*. **2008**, 3, 210–215.

[88] Schönhoff, M. *J. Phys. Condens. Matter* **2003**, 15, 1781–1808.

[89] Dubas, S. T.; Schlenoff, J. B. *Macromolecules* **1999**, 32, 8153–8160.

[90] Bard, A. J.; Faulkner, L. R. Electrochemical Methods: Fundamentals and Applications; 2nd ed.; Wiley: New York, 1980; p. 833.

[91] Elzbieciak, M.; Kolasinska, M.; Warszynski, P. *Colloids Surfaces A Physicochem. Eng. Asp*. **2008**, 321, 258–261.

[92] Durstock, M. F.; Rubner, M. F. *Langmuir* **2001**, 17, 7865–7872.

[93] Stern, E.; Wagner, R.; Sigworth, F. J.; Breaker, R.; Fahmy, T. M.; Reed, M. A. *Nano Lett*. **2007**, 7, 3405–3409.

[94] Stern, E.; Klemic, J. F.; Routenberg, D. A.; Wyrembak, P. N.; Turner-Evans, D. B.; Hamilton, A. D.; LaVan, D. A.; Fahmy, T. M.; Reed, M. A. *Nature* **2007**, 445, 519–522.

[95] Kolasińska, M.; Krastev, R.; Warszyński, P. J. *Colloid Interface Sci*. **2007**, 305, 46–56.

[96] Wei, P.; Liu, N.; Lee, H. R.; Adijanto, E.; Ci, L.; Naab, B. D.; Zhong, J. Q.; Park, J.; Chen, W.; Cui, Y.; Bao, Z. *Nano Lett*. **2013**, 13, 1890–1897.